ABSTRACT

EFFICIENT APPROXIMATIONS FOR STATIONARY SINGLE-CHANNEL CALCIUM NANODOMAINS

by
Yinbo Chen

Mathematical and computational modeling plays an important role in the study of local Ca^{2+} signals underlying many fundamental physiological processes such as synaptic neurotransmitter release and myocyte contraction. Closed-form approximations describing steady-state distribution of Ca^{2+} in the vicinity of an open Ca^{2+} channel have proved particularly useful for the qualitative modeling of local Ca^{2+} signals. This dissertation presents several simple and efficient approximants for the equilibrium Ca^{2+} concentration near a point source in the presence of a mobile Ca^{2+} buffer, which achieve great accuracy over a wide range of model parameters. Such approximations provide an efficient method for estimating Ca^{2+} and buffer concentrations without resorting to numerical simulations and allow to study the qualitative dependence of nanodomain Ca^{2+} distribution on the buffer's Ca^{2+} binding properties and its diffusivity. The new approximants presented here for the case of a simple, one-to-one Ca^{2+} buffer have a functional form that combines rational and exponential functions, which is similar to that of the well-known Excess Buffer Approximation and the linear approximation, but with parameters estimated using two novel methods. One of the methods involves interpolation between the short-range Taylor series of the buffer concentration and its long-range asymptotic series in inverse powers of distance from the channel. A second method is based on the variational approach and involves a global minimization of an appropriate functional with respect to parameters of the chosen approximations. Extensive parameter sensitivity analysis is presented,

comparing approximants found using these two methods with the previously developed approximants. Apart from increased accuracy, the strength of the new approximants is that they can be extended to more realistic buffers with multiple Ca^{2+} binding sites, such as calmodulin and calretinin. In the second part of the dissertation, the series interpolation method is extended to buffers with two Ca^{2+} binding sites, yielding closed-form interpolants combining exponential and rational functions that achieve reasonable accuracy even in the case of buffers characterized by significant Ca^{2+} binding cooperativity. Finally, open challenges and potential future extensions of this work are discussed in detail.

EFFICIENT APPROXIMATIONS FOR STATIONARY SINGLE-CHANNEL CALCIUM NANODOMAINS

by
Yinbo Chen

A Dissertation
Submitted to the Faculty of
New Jersey Institute of Technology
and Rutgers, The State University of New Jersey – Newark
in Partial Fulfillment of the Requirements for the Degree of
Doctor of Philosophy in Mathematical Sciences

Department of Mathematical Sciences, NJIT
Department of Mathematics and Computer Science, Rutgers-Newark

August 2020

APPROVAL PAGE

EFFICIENT APPROXIMATIONS FOR STATIONARY SINGLE-CHANNEL CALCIUM NANODOMAINS

Yinbo Chen

Dr. Victor V. Matveev, Dissertation Advisor — Date
Professor of Mathematical Sciences, NJIT

Dr. Cyrill Muratov, Committee Member — Date
Professor of Mathematical Sciences, NJIT

Dr. Casey O. Diekman, Committee Member — Date
Associate Professor of Mathematical Sciences, NJIT

Dr. Denis L. Blackmore, Committee Member — Date
Professor of Mathematical Sciences, NJIT

Dr. Arthur Sherman, Committee Member — Date
Chief, Lab. of Biol. Modeling, NIDDK, NIH, Bethesda, MD

BIOGRAPHICAL SKETCH

Author: Yinbo Chen

Degree: Doctor of Philosophy

Date: August 2020

Undergraduate and Graduate Education:

- Doctor of Philosophy in Mathematical Sciences,
  New Jersey Institute of Technology, Newark, NJ, 2020

- Bachelor of Science in Biology,
  Shaanxi Normal University, Xi'an, Shaanxi, 2011

Major: Mathematical Sciences

Presentations and Publications:

Chen, Y., C. Muratov, and V. Matveev. "Efficient approximations for stationary single-channel Ca^{2+} nanodomains across length scales", bioRxiv. 23: 2020.01.16.909036, 2020. (Biophys. J. In Press)

Chen, Y., and V. Matveev, "Approximation of stationary Ca^{2+} nanodomains in the presence of cooperative Ca^{2+} buffers", Poster Presentation, 29th Annual Computational Neuroscience Meeting, Online, 2020.

Chen, Y., and V. Matveev, "Padé approximation of single-channel calcium nanodomains in the presence of cooperative calcium buffers", Poster Presentation, 63rd Biophysical Society Meeting, Baltimore, MD, 2019.

Chen, Y., C. Muratov, and V. Matveev, "Stationary approximations to single-channel Ca^{2+} nanodomains", Poster Presentation, 2nd Annual Institute for Brain and Neuroscience Research (IBNR) Graduate Student/Postdoctoral Research Showcase, NJIT, 2019.

Chen, Y., and V. Matveev, "Padé approximation of stationary Ca^{2+} nanodomains in the presence of cooperative Ca^{2+} buffers", Poster Presentation, 1st Annual Institute for Brain and Neuroscience Research (IBNR) Graduate Student/Postdoctoral Research Showcase, NJIT, 2018.

Chen, Y., X. Li, H. G. Rotstein, and F. Nadim, "Membrane potential resonance frequency directly influences network frequency through electrical coupling", J. Neurophysiol. 116(4):1554-1563, 2016.

This dissertation is dedicated to my wife and my parents.

ACKNOWLEDGMENT

Pursuing a Ph.D. degree really is a lot more about the journey than the end, and I could not have made through mine so joyfully without the support from many people. Here, I would like to mention those people who made this journey an unforgettable experience for me.

I would like to express my deepest gratitude to my mentor and friend, Dr. Victor Matveev, for his excellent guidance, caring, patience, and providing me with an excellent friendly atmosphere for research. I am always grateful for his trust, his encouragement and his believing in my potential. What he taught me is not limited to the research studies but also how to be an independent researcher. It has been an honor and a pleasure to study under the supervision of such an individual of exceptional professional, teaching and personal qualities.

I also wish to show my gratitude to the rest of my dissertation committee members, Dr. Cyrill Muratov, Casey Diekman, Denis Blackmore, and Arthur Sherman for their guidance and helpful suggestions during my research, especially Dr. Cyrill Muratov, who contributes enormously on the theoretical component of my dissertation.

I am grateful to my parents, Junmei Liu and Zhenwu Chen, for their unwavering faith, love, and confidence in me and in my abilities – they have shaped me into the person that I am today. Thank you very much for everything.

I would like to thank the Department of Mathematical Sciences of NJIT for giving me the opportunity to pursue a Ph.D. degree at such a prestigious university and for understanding the need of its graduate students. I also acknowledge the support by NSF Grant DMS-1517085.

Most importantly, I would like to pay my regards to the one person to whom I owe everything that I am today: my wife, Haoying Ke, who has been my strength, and my weakness. A thank you is not enough for all the support, encouragement, and unconditional love that she has given me, and I cannot wait to start our new life together once I graduate.

And finally, I would like to thank my late Grandmother, Lijuan Dai, who raised me when I was a child. I wish she was here with me on this special day of my life.

TABLE OF CONTENTS

TABLE OF CONTENTS
(Continued)

LIST OF TABLES

LIST OF TABLES
(Continued)

LIST OF FIGURES

LIST OF FIGURES
(Continued)

LIST OF FIGURES
(Continued)

Figure **page**

LIST OF FIGURES
(Continued)

Figure **page**

LIST OF FIGURES
(Continued)

Figure **page**

LIST OF FIGURES
(Continued)

Figure **page**

CHAPTER 1

INTRODUCTION

Some of the most fundamental physiological cell processes such as synaptic neurotransmitter release, endocrine hormone release, muscle contraction and cytotoxic immune cell response are directly and quickly triggered by the Ca^{2+} influx into the cytoplasm through transmembrane Ca^{2+} channels (1-4). Due to the diversity of Ca^{2+}-controlled cellular processes, intracellular Ca^{2+} signals are localized in time and space to allow selective activation of specific reactions (2-5). This localization is maintained in part by intracellular Ca^{2+} buffers, which absorb most of the Ca^{2+} influx soon upon its entry into the cell (6, 7). In the context of secretory vesicle exocytosis, local Ca^{2+} concentration elevations around individual Ca^{2+} channels or clusters of channels are termed Ca^{2+} nano- or micro-domains (4, 8). Although Ca^{2+} concentration can be measured experimentally using Ca^{2+} sensitive dyes, inherent physical limitations pose challenges for optical Ca^{2+} imaging on small temporal and spatial scales relevant for vesicle exocytosis and other processes controlled by local Ca^{2+} elevations. Therefore, mathematical and computational modeling has played an important role in the study of vesicle exocytosis and other cell processes activated by localized Ca^{2+} signals (8-15). In particular, these computational studies were instrumental in showing that local Ca^{2+} elevations form and collapse very rapidly in response to channel gating. This suggests that quasi-stationary solutions of the reaction-diffusion equations describing Ca^{2+} influx, diffusion and binding to intracellular Ca^{2+} buffers may achieve sufficient accuracy in estimating Ca^{2+} concentration in the vicinity of a Ca^{2+} channel, obviating computationally expensive solutions of partial differential equations describing buffered Ca^{2+} diffusion (16, 17).

Several of such stationary approximations have been introduced in the early works of Neher, Stern, Keizer, Smith and others (14, 18-28), most notably the Excess Buffer approximation (EBA), the Rapid Buffering approximation (RBA), and the linear approximation (LIN) (see Table 2.1). These approximations proved quite useful in understanding the properties of Ca^{2+} nanodomains and their dependence on the properties of cell Ca^{2+} buffers, and are widely used in modeling studies (9, 14, 21, 29-32). However, most of the previously developed approximations have two limitations: (1) their accuracy is restricted to specific regions in buffering parameter space corresponding to small values of appropriate non-dimensional quantities, and (2) they have been developed for simple, one-to-one Ca^{2+}-buffer binding, and are hard to extend to buffers that have multiple Ca^{2+} binding sites (33). However, many biological Ca^{2+} buffers do have multiple binding sites. For example, many widely expressed buffers such as calretinin and calmodulin, which play a prominent role in a variety of fundamental physiological processes, are characterized by two-site molecular EF-hand domains with cooperative Ca^{2+} binding, whereby the binding of a second Ca^{2+} ion proceeds with much greater affinity once the first binding site is occupied (35-42). In previous studies, only RBA has been extended to such realistic buffers, but its accuracy is very sensitive to model parameters (33). Further, other methods such as LIN are simply not applicable to complex buffers.

Addressing the challenges noted above is the main goal of the work presented in this dissertation. Therefore, our aims are two-fold: (1) develop new methods for estimating Ca^{2+} nanodomains with more uniform accuracy with respect to the broadest possible range of modeling parameters, and (2) extend the newly developed approaches to approximate Ca^{2+} nanodomains in the presence of Ca^{2+} buffers with two binding sites.

In Chapter 2, we tackle the first of our main goals, presenting new approaches and new approximants allowing to better approximate single-channel Ca^{2+} nanodomains with more accuracy and for a wider range of model parameters in the case of simple one-to-one buffers. One of these approximation methods is based on matching the coefficients of short-range Taylor series and long-range asymptotic series of the nanodomain Ca^{2+} distance dependence using simple *ansätze*. Although this method has already been used to obtain Padé (rational function) nanodomain approximations (34), we show that significant improvement can be achieved in some parameter regimes using alternative interpolants that are similar in their functional form to EBA and LIN approximants shown in Table 2.1. Apart from the series interpolation approach, which can be categorized as a local approach, we also present a different class of methods based on the variational approach, which involve a global optimization of a relevant functional with respect to parameters of the same *ansätze* that we use with the series interpolation method. As we will demonstrate, approximants achieved using this alternative, global approach achieve superior accuracy with respect to all other methods in a significant portion of the relevant parameter space.

In Chapter 3 of this dissertation, we address the second of our main goals by showing that the series interpolation methods can be extended to buffers with two binding sites, using simple *ansätze* similar to those considered in Chapter 2. We systematically explore the parameter dependence of the accuracy of the new methods, and demonstrate that the new approximants we introduce significantly improve approximation accuracy as compared to RBA in a wide range of parameter regimes.

Finally, in Chapter 4, we summarize our results, and outline many potential directions for improvement and for possible future extensions of this work.

CHAPTER 2

SIMPLE BUFFER CASE

2.1 Methods: Single-channel Ca^{2+} Nanodomain Equation

Following prior work, we will consider a Ca^{2+} buffer whose molecules possess a single active site that binds a Ca^{2+} ion according to the reaction

$$B + Ca^{2+} \underset{k^-}{\overset{k^+}{\rightleftharpoons}} B^*. \tag{2.1}$$

Here B and B^* are the free buffer and Ca^{2+}-bound buffer, respectively, and k^+/k^- are the Ca^{2+}-buffer binding/unbinding rates. We consider a semi-infinite diffusion domain bounded by a flat plane containing point Ca^{2+} channel sources. Following previous modelling studies (18, 19, 27), we will assume Dirichlet boundary conditions on the outer boundary representing the background concentrations for Ca^{2+} and buffer in the bulk of the cell cytoplasm, and zero flux boundary condition on the flat boundary representing the cell membrane. Although this neglects Ca^{2+} pumps and exchangers along the flat boundary, numerical simulations show that qualitative agreement with more accurate models is retained under this assumption. The reflection symmetry along the flat boundary allows to extend the domain to the whole space, while doubling the source strength. Assuming mass-action kinetics, this yields the following reaction-diffusion system in $\mathbb{R}^3$ (18, 19):

$$\begin{aligned}
\partial_t C &= D_C \nabla^2 C - k^+ B C + k^- B^* + 2\sum_{k=1}^{N_{Ca}} \sigma_k \, \delta(\mathbf{r} - \mathbf{r}_k), \\
\partial_t B &= D_B \nabla^2 B - k^+ B C + k^- B^*, \\
\partial_t B^* &= D_B^* \nabla^2 B^* + k^+ B C - k^- B^*.
\end{aligned} \tag{2.2}$$

Here C, B and B^* represents concentrations of Ca^{2+}, free buffer and Ca^{2+}-bound buffer, respectively, with diffusivities D_C, D_B, and D_B^*. In the source term, N_{Ca} denotes the number of Ca^{2+} channels, and the source strengths are given by $\sigma_k = I_{Ca,k}/(z\,F)$, where $I_{\mathrm{Ca,k}}$ are the amplitudes of individual open Ca^{2+} channels located at positions $\mathbf{r}_k$, F is the Faraday constant, and z=2 is the valence of the Ca^{2+} ion. We note that the point-like channel assumption introduces inaccuracy at small spatial scales commensurate with the channel pore width of several nanometers. The impact of finite channel diameter and volumetric Ca^{2+} clearance was considered in a different type of single-channel stationary solution derived for the endoplasmic reticulum Ca^{2+} channel in (16).

The two linear combinations of Equation 2.2 that cancel the reaction terms yield the conservation laws for the total Ca^{2+} and total buffer concentrations:

$$\partial_t \left(C + B^* \right) = \nabla^2 \left(D_C C + D_B^* B^* \right) + 2\sum_{k=1}^{N_{Ca}} \sigma_k \, \delta(\mathbf{r} - \mathbf{r}_k), \tag{2.3}$$

$$\partial_t \left(B + B^* \right) = \nabla^2 \left(D_B B + D_B^* B^* \right). \tag{2.4}$$

We now consider the steady state of this system, where the conservation laws for Ca^{2+} and buffer reduce to (19-21, 27, 43, 44):

$$D_B B + D_B^* B^* = D_B B_\infty + D_B^* B_\infty^* = const\,. \tag{2.5}$$

$$\nabla^2 \left[D_C C + D_B^* B^* \right] = -2 \sum_{k=1}^{N_{Ca}} \sigma_k \, \delta(\mathbf{r} - \mathbf{r}_k)\,. \tag{2.6}$$

Our approach is somewhat more general than prior modeling work in that we do not assume that buffer mobility is unaffected by Ca^{2+} binding. Given our simplifying assumptions on the domain geometry and boundary conditions, Equation 2.6 has an exact solution:

$$D_C C + D_B^* B^* = \frac{1}{2\pi} \sum_{k=1}^{N_{Ca}} \frac{\sigma_k}{|\mathbf{r} - \mathbf{r}_k|} + D_C C_\infty + D_B^* B_\infty^*, \tag{2.7}$$

where C_∞ and B_∞ are the background Ca^{2+} and buffer concentrations infinitely far from the channel, which are in equilibrium with each other:

$$B_\infty C_\infty = K\, B_\infty^*\,. \tag{2.8}$$

Here $K = k^- / k^+$ is the buffer affinity, equal to the Ca^{2+} concentration at which half the buffer is bound at steady state. Conservation laws allow to eliminate two variables, and we choose to retain the equilibrium unbound buffer concentration as the remaining unknown:

$$D_B \nabla^2 B = k^+ B C - k^- B^*\,. \tag{2.9}$$

We will now non-dimensionalize these equations in a manner similar to the method of Smith et al (19) (see also (34)), rescaling Ca^{2+} by the buffer affinity: $c=C/K$, $c_\infty=C_\infty/K$. However, we normalize the buffer concentration by its background value B_∞ instead of total concentration. This will simplify analytic results, with many expressions formally unchanged whether or not $c_\infty=0$ (see Table 2.1). Note also that in this case a very simple relationship holds between background concentrations of Ca^{2+} and bound buffer: Equation 2.8 yields $c_\infty = b^*_\infty$.

We will consider the case of a single channel at the origin, and re-scale the spatial coordinate ($\mathbf{r}/L \to \mathbf{r}$) using the scale parameter that depends on the strength of the Ca^{2+} current, which simplifies the source term in Equation 2.7 (19):

$$L = \sigma \Big/ \left(2\pi D_C K\right). \tag{2.10}$$

Recalling that $c_\infty = b^*_\infty$, we obtain the following non-dimensional form of free buffer dynamics given by Equation 2.9, and the conservation laws, Equations 2.5, 2.7:

$$\begin{cases} \lambda \nabla^2 b \ = bc - b^*, \\ b + \delta^*_B b^* = 1 + \delta^*_B c_\infty, \\ c + \nu \delta^*_B b^* = c_\infty + \nu \delta^*_B c_\infty + 1/|\mathbf{r}|, \end{cases} \tag{2.11}$$

where the 4 non-dimensional model parameters are (with L given by Equation 2.10):

$$\lambda = \frac{D_B}{L^2 k^-}; \quad \nu = \frac{B_\infty D_B}{K D_C}; \quad \delta^*_B = \frac{D^*_B}{D_B}; \quad c_\infty = \frac{C_\infty}{K}. \tag{2.12}$$

Here λ is the dimensionless buffer diffusion coefficient (denoted as ε_b in (19)), which quantifies the diffusion rate relative to the rate of Ca^{2+} binding and influx, while ν (denoted as $1/\mu$ in (19)) represents the overall buffering strength at rest, given by the product of the resting buffering capacity (B_∞/K) and the relative buffer mobility (D_B/D_C). In this non-dimensionalization, the unbuffered Ca^{2+} solution corresponds to ν=0 and has a particularly simple form, $c = 1/|\boldsymbol{r}| + c_\infty$. For the sake of simplicity, we will also use the following auxiliary parameters:

$$\eta = c_\infty + \frac{1}{\delta_B^*}, \quad q = \frac{1}{\eta + \nu}. \tag{2.13}$$

This allows to specify the problem using only three parameters, either $\{\lambda, \nu, \eta\}$ or $\{\lambda, q, \eta\}$. In the special case of binding-independent buffer mobility ($\delta_B^* = 1$), the parameter η equals the non-dimensionalized total buffer concentration: $b_T = (B_\infty + B_\infty^*) / B_\infty = 1 + c_\infty = \eta$.

Eliminating the bound buffer and Ca^{2+} concentrations using the two conservation laws in Equation 2.11, the free buffer equation takes on a simple form:

$$\lambda \nabla^2 b = (b-1)(\nu b + \eta) + \frac{b}{|\mathbf{r}|}. \tag{2.14}$$

The Ca^{2+} concentration can be obtained from the solution of Equation 2.14 using the Ca^{2+} conservation law in Equation 2.11, which can be simplified to the following intuitive form:

$$c = \nu(b-1) + c_\infty + \frac{1}{|\mathbf{r}|}. \tag{2.15}$$

For $b<1$, the Ca^{2+} concentration is reduced in proportion to the buffering strength parameter ν, as expected. The conservation laws in Equation 2.11 along with the physical constraints $c\geq 0$, $b^*\geq 0$, $c_\infty \geq 0$ imply *a priori* bounds

$$\begin{aligned} &b_-(\mathbf{r}) \leq b(\mathbf{r}) \leq b_+(\mathbf{r}), \\ &b_-(\mathbf{r}) = \max\left(0, 1 - \frac{1}{\nu|\mathbf{r}|} - \frac{c_\infty}{\nu}\right), \\ &b_+(\mathbf{r}) = 1 + \delta_B^* c_\infty. \end{aligned} \tag{2.16}$$

The solutions satisfy the following boundary conditions (here and below, we denote $r = |\mathbf{r}|$):

$$\begin{cases} \lim\limits_{|\mathbf{r}|\to 0} b(\mathbf{r}) = b_0 = \text{const}, \\ \lim\limits_{|\mathbf{r}|\to +\infty} b(\mathbf{r}) = 1, \end{cases} \tag{2.17}$$

where the value of buffer at the source location, b_0, is unknown *a priori*. As is regorously proved in (48) (see Appendix 4 therein), Equation 2.14 has a unique solution which is bounded and satisfies the boundary conditions shown in Equation 2.17, and this solution is spherically symmetric. Therefore, Equation 2.14 may be reduced to

$$E[b] \equiv -\frac{\lambda}{r^2}\frac{d}{dr}\left(r^2\frac{db}{dr}\right)+(b-1)(\nu b+\eta)+\frac{b}{r}=0\,. \tag{2.18}$$

Although Equation 2.18 superficially resembles the Lane–Emden-Fowler equations (45), it has no local Lie symmetries allowing analytical solution. Further, it is not of Painlevé type (46), despite its simple algebraic form. We carried out the numerical solution of Equation 2.18 using the relaxation method and the shooting method, cross-validating the results of these two methods. For certain extreme values of the model parameters, accurate numerical solution is computationally intensive.

We note that the chosen non-dimensionalization is identical to the one in (19, 34) in the case of binding-invariant buffer mobility ($\delta_B^* = 1$) and zero background Ca^{2+} concentration (c_∞=0). In the case $c_\infty \neq 0$ there is a simple equivalence with the non-dimensionalization in (19, 34); indicating variables and parameters in the latter work with the hat symbol, this equivalence reads:

$$\nu = \hat{b}_\infty \hat{\nu}\ ,\ \hat{b} = \frac{b}{\eta}\ ,\ \ \hat{b}_\infty = \frac{1}{\eta}. \tag{2.19}$$

Most numerical results shown below focus on the special case c_∞=0, $\delta_B^* = 1$, corresponding to η=1 (Figures 2.1-2.6). The results for η=10 are also shown, in the results summary Figure 2.7.

Table 2.1 Previously Established Single-channel Equilibrium Ca^{2+} Nanodomain Approximations. For each method, only the free buffer concentration expression is shown, since the non-dimensional Ca^{2+} concentration can be found from the Ca^{2+} conservation law (Equation 2.15), with the exception of terms in 2nd-order EBA, which are given in (19). Note that LIN and EBA become identical in the limit $\nu>>1$. RBA approximations valid up to orders O(1) and O(λ) are denoted as 1st-order RBA (or simply RBA) and 2nd-order RBA (RBA2), respectively. Two lowest orders of the Padé method are denoted Padé for the 1st order case, and Padé2 for the 2nd order case. For Padé2, the parameter-dependent rational function constants $A_{1,2}$ and $B_{1,2}$ are given by the solution of a 4th order polynomial equation (34), which has a closed-form solution shown in Appendix C.

Method	**Free buffer concentration, $b(r)$**	**Conditions**	**Refs**
LIN	$1+\frac{q}{r}\left[\exp\left(-r/\sqrt{q\lambda}\right)-1\right]$	Linearization around b=1	(14, 19, 22, 23, 25, 26)
EBA	$1+\frac{1}{\nu r}\left[\exp\left(-r\sqrt{\nu/\lambda}\right)-1\right]+O\left(\frac{1}{\nu^2}\right)$	$\lambda>>1,\ \nu>>1,$ $\lambda/\nu=O(1)$	(14, 19, 28)
IBA	$\eta\left[\frac{r}{1+\eta r}+\frac{\nu r^2}{(1+\eta r)^3}+\frac{2\lambda}{(1+\eta r)^4}\right]$	$\lambda<<1,\ \nu<<1,$ $\lambda/\nu=O(1)$	(19)
RBA	$1-\frac{1}{2q\nu}\left[1+\frac{q}{r}-\sqrt{\left(1+\frac{q}{r}\right)^2-\frac{4\nu q^2}{r}}\right]$	$\lambda<<1,\ \nu=O(1)$	(14, 18-21, 29)
RBA2	$b_{RBA}(r)+2\lambda\eta\left[\left(1+\frac{r}{q}\right)^2-4\nu r\right]^{-2}$	$\lambda<<1,\ \nu=O(1)$	(19)
Padé	$1-\frac{q}{r+\left[\sqrt{q(q+8\lambda)}+q\right]/2}$	Series interpolation	(34)
Padé2	$\frac{r^2+A_1(\lambda,\nu,\eta)r+A_2(\lambda,\nu,\eta)}{r^2+B_1(\lambda,\nu,\eta)r+B_2(\lambda,\nu,\eta)}$	Series interpolation	(34)

One of the contributions of early modeling efforts was the development of accurate analytical approximations of the solution of Equation 2.18. They allow avoiding computationally expensive integration of reaction-diffusion equations while retaining considerable accuracy (19, 34). These approximations are summarized in Table 2.1, and apart from the Padé and LIN approximants, their regimes of applicability can be explained in intuitive physical terms. Namely, the Excess Buffer Approximation (EBA) is applicable when the buffer concentration is so large that it is practically unsaturable by the given Ca^{2+} current, leading to an additional exponential decay factor for the Ca^{2+} concentration with increasing distance from the channel (14, 19, 28). The Rapid Buffering Approximation (RBA) corresponds to the parameter regime where the buffering rate is much faster relative to the diffusion rate, and at lowest order represents the condition for instantaneous equilibrium of the Ca^{2+} buffering reaction (14, 18-21, 29). The nearly immobile buffer approximation (IBA) is applicable in the case of small buffer mobility, implying in turn a weak buffering strength (19). Finally, the linear approximation (LIN) represents an *ad hoc* linearization around the free unbuffered point-source solution, $b = 1$, $c = 1/r + c_\infty$, but as Table 2.1 shows, LIN could also be viewed as an improved modification of the EBA. More precise meaning of these approximants was given in Smith et al. (19). The latter work showed that EBA, RBA and IBA represent asymptotic expansions in either λ or $\mu=1/\nu$, and provided such expansions up to 2nd order with respect to these parameters. In contrast, the Padé approximation (34) is based on a series matching method explained in detail below. We note that only 2nd order RBA and Padé approximations are comparable in accuracy to the approximants presented in this work. Since $[Ca^{2+}]$ is uniquely determined by the buffer concentration through the conservation law (Equation 2.15), $[Ca^{2+}]$

estimation accuracy is only shown in the final summary and comparison of all approximations (see Figures 2.5-2.7). We note that accurate estimation of free buffer concentration can be as important as the knowledge of the corresponding Ca^{2+} concentration, since it helps in the understanding of cell Ca^{2+} homeostasis, and in interpreting the results of Ca^{2+} imaging, which requires quantifying Ca^{2+} binding to exogenously applied fluorescent Ca^{2+} buffers (2, 3, 5, 8).

2.2 Local Properties of Stationary Nanodomain Solution

We start by generalizing some of the results previously presented in (34), without the restriction of binding-independent buffer mobility. We seek a solution to Equation 2.18, which is bounded and analytic, and therefore it can be expanded in a Taylor series in r using a Frobenius-like method (justification is given in Appendix G):

$$b(r) = b_o + \frac{b_o}{2\lambda} r + \frac{(b_0 - 1)(\nu b_o + \eta) + b_o/(2\lambda)}{6\lambda} r^2 + O(r^3). \tag{2.20}$$

The usefulness of this series by itself is limited since the value of buffer at the channel location, b_o, is *a priori* unknown, as mentioned above. Further, the convergence radius is finite due to possible movable non-pole singularities of the solution in the complex r plane. However, the relationship between Taylor coefficients in this expansion can be used to constrain parameters of an appropriately chosen approximation. Further, by making a coordinate mapping $x \equiv 1/r$, we transform our original Equation 2.18 to the form:

$$\lambda x^4 b_{xx} = (b-1)(\nu b + \eta) + bx. \tag{2.21}$$

This reveals an essential singularity at x=0. In fact, numerical study shows that the analytic extension of $b(x)$ to the complex-x plane has a branch cut across x=0, jumping from the physical value b=1 at $x=0^+$ ($r = +\infty$) to the unphysical value $b = -\eta/\nu$ at $x=0^-$ ($r = -\infty$) (see Figure 7 in (34)).

Given that the boundary condition infinitely far from the channel is known, $b(x=0^+)=1$, one can readily find the coefficients of a unique asymptotic power series expansion near $x=0^+$:

$$b(x) = 1 - qx + \eta q^3 x^2 + \eta(1 - 2q\eta) q^4 x^3 + \eta\left(2\lambda + 5\eta q^2 (\eta q - 1)\right) q^4 x^4 + O(x^5). \qquad (2.22)$$

Here we used parameter $q = 1/(\eta+\nu)$ to simplify the coefficients (cf. Equation 16 in (34)). Note that terms of this long-range expansion agree up to order $O(x^3)$ with RBA and up to order $O(x^5)$ with RBA2 (Table 2.1), indicating that the reaction is approximately at equilibrium far from channel.

The Padé method introduced in (34) and shown in Table 2.1 simultaneously matches leading terms of the two expansions given by Equations 2.20 (containing unknown b_0 as a free parameter) and 2.22, using a simple rational function interpolant, with coefficients of this rational function found as functions of model parameters λ, ν (or q), and η. The simplest Padé interpolant of order 1 yields:

$$b(r) = 1 - \frac{q}{r + B}, \text{ where } B = \frac{1}{2}\left[q + \sqrt{q(q + 8\lambda)}\right]. \qquad (2.23)$$

This function satisfies both $b(r) = b_0 + b_0 r / 2\lambda + O(r^2)$ and $b(x) = 1 - qx + O(x^2)$. The corresponding estimate of free buffer concentration at the channel location is $b_0 = 1 - q/B$.

The Padé approximation (see Table 2.1) was chosen in (34) because of its algebraic simplicity and its straightforward expansion in power series in both *r* and $x=1/r$. Therefore, it represents an *ad hoc ansatz*, and for a fixed polynomial order, it is not necessarily the most natural nor the most accurate interpolant between the short-range and long-range power series given by Equations 2.20-2.22. Further, although it does converge to the true solution with increasing order, closed-form expressions for its coefficients can only be obtained for the two lowest orders listed in Table 2.1. However, we observe that *all* approximants in Table 2.1 can be viewed as interpolants between the Taylor series in *r* and asymptotic power series in $x=1/r$, and therefore the series interpolation method first introduced in (34) can and should be applied to the corresponding functional forms, as well. Particularly promising in this respect is the simple exponential form of the EBA and LIN approximations, which are close to each other when $\nu \gg 1$, and which match in this limit the first two terms in the asymptotic expansion in Equation 2.22, $b(x) = 1 - qx + O(x^2)$. In fact, standard analysis by substitution $b(x) = 1 - qx + e^{S(x)}$ reveals that in the limit $x = 1/r \to 0^+$, the behavior of the general solution to Equation 2.21 is described by:

$$b(x) = 1 - qx + \eta q^3 x^2 + \ldots + C(x) x^{1+\sqrt{\frac{q}{\lambda}}\left(q-\frac{1}{2}\right)} e^{-\frac{1}{x\sqrt{q\lambda}}}, \tag{2.24}$$

where $C(x)$ is bounded at $x=0$. Apart from the fractional power of x, this expression has a similar form to the EBA and LIN approximations in Table 2.1, suggesting that the

corresponding functional form is a natural *ansatz* for describing long-range behavior of the solution.

2.3 Results

2.3.1 Functional Form of Approximants

Given above analysis, we introduce approximants that have a simple functional form inspired by EBA and LIN, and which match the long-range asymptotic behavior of the solution, as given by Equation 2.24. Namely, we consider approximations in one of the following three parametric forms:

$$b(r) = 1 + q\frac{e^{-\alpha r} - 1}{r}, \tag{2.25}$$

$$b(r) = 1 + q\frac{e^{-\alpha r} - 1}{r} - q^3\eta\frac{e^{-\alpha r}(1+\alpha r) - 1}{r^2}, \tag{2.26}$$

$$b(r) = 1 + q\frac{e^{-\alpha r} - 1}{r} + q^3\eta\frac{1}{\beta + r^2}. \tag{2.27}$$

We refer to these approximants as exponential (Exp), double exponential (DblExp), and exponential-Padé (Exp-Padé), respectively. In the limit $r \to +\infty$ (x=1/r $\to 0^+$), they explicitly satisfy the asymptotic expansion $b(x) = 1 - qx + \eta\, q^3x^2 + O(x^3)$ to either 1st or 2nd order in x, and are analytic at $r = 0$. The Exp and DblExp approximants depend on a single parameter α, while Exp-Padé contains an additional parameter β. Note that Equation 2.25 reduces to LIN or EBA when α equals $1/\sqrt{q\lambda}$ or $1/\sqrt{\mu\lambda}$, respectively (see

Table 2.1). The novelty of our approach is that we constrain the values of parameters α and β using one of the following methods, described in detail further below:

1. Series interpolation: in this case approximants given by Equations 2.25, 2.26 are referred to as Exp-Ser and DblExp-Ser, respectively.
2. Variational approach: Equations 2.25, 2.26 in this case are referred to as Exp-Var and DblExp-Var.
3. Global method (modified variational approach): Equations 2.25, 2.26 will be called Exp-Global and DblExp-Global.

The value of parameter α is given by the solution of a quadratic equation for the exponential *ansatz*, and cubic equation for the double exponential *ansatz*, as given in Table 2.2. Parameters of the Exp-Padé approximant are defined by a 4th-order polynomial equation, and are explicitly shown in Appendix B.

2.3.2 Series Interpolation Approach

For the simple exponential *ansatz*, Equation 2.25, the relationship between the first two coefficients in the Taylor series in Equation 2.20, $b_1 = b_0 / 2\lambda$, is satisfied for a unique value of exponent factor α given by a root of a quadratic equation, and listed in Table 2.2: $\alpha = \left(\sqrt{1+4\lambda/q}-1\right)\Big/\left(2\lambda\right)$. The corresponding approximant will be referred to as Exp-Ser, in contrast to LIN, which has the same functional form, but with the exponent factor value of $\alpha = 1/\sqrt{q\lambda}$ (cf. Table 2.1).

A slightly more complex expression in terms of two exponentials, Equation 2.26, allows to match two terms in the long-range asymptotic x-power series, $1 - qx + \eta q^3\, x^2 + O(x^3)$. The relationship between the first two coefficients in the Taylor series in Equation 2.20, $b_1 = b_0 / 2\lambda$, holds when the value of exponent factor α satisfies a cubic equation given in Table 2.2. This cubic has at most one real positive root for all values of

model parameters $\{\lambda, q, \eta\}$, which has an explicit solution shown in Appendix A. The correspoding approximant will be referred to as DblExp-Ser. We note that α becomes imaginary for sufficiently small λ and ν, inside a parameter region marked by thin lines in Figure 2.6A1, A2; in that case the real part of Equation 2.26 will be used to compare it with other methods.

Finally, the *ansatz* given by Equation 2.27 has an exponential term with parameter α, and a rational term with parameter β. Two free parameters allow to match two relationships between the first three Taylor coefficients in the short-range series expansion given by Equation 2.20. This results in a polynomial system of order 4, with the level of complexity similar to that of the second-order Padé approximation (34). This polynomial system and the explicit expression for its roots are provided in Appendix B. We note that the real positive solution for parameters α and β is only possible when $\nu<\eta$ (equivalently, $2\eta q > 1$), so this approximation is not applicable for $\nu>\eta$.

Table 2.2 Equations for Determining *Ansatz* Exponent Parameter α. The approximants given by Equations 2.25 and 2.26 depend on a single constant exponent factor α that in turn depends on model parameters λ, $q=(\nu+\eta)^{-1}$ and η through the solution of a quadratic or a cubic equation. For all three mono-exponential approximants (Exp-Ser, Exp-Var, Exp-Global), the value of α is given by a solution to a quadratic equation of the same kind, but with different values of parameter S. Note that setting $S=0$ yields the linear approximation (LIN in Table 2.1). For all three double-exponential approximants (DblExp-Ser, DblExp-Var, DblExp-Global), the value of parameter α is given by a solution to a cubic equation of the same type, shown in the top row of the table, but with different values of polynomial coefficients P, Q, and R. There is at most one positive real root of the cubic equation, which is given in Appendix A.

	Exp (Exponential)	**DblExp (Double-Exponential)**
	$\alpha = \left(\sqrt{S^2 + \lambda/q} - S\right) \Big/ \lambda$	$\eta q^2 P \alpha^3 - Q\alpha^2 - R\alpha + 1/q = 0$
Series interpolation	**Exp-Ser** $S = 1/2$	**DblExp-Ser** $P = 2\lambda/3,\ \ Q = \lambda - q^2\eta/2,\ \ \ R = 1.$
Variational method	**Exp-Var** $S = \left(1 + 2q\eta\right)/3$	**DblExp-Var** $P = \lambda\left(8\ln 2 - 5\right) + 4q^2\eta\left(1 - \eta q\right)\left(\frac{1}{3} - \ln\frac{4}{3}\right),$ $Q = \lambda + \frac{2}{3}q^2\eta\left[1 - 6\ln\frac{9}{8} + 2q\eta\left(1 - 6\ln\frac{4}{3}\right)\right],$ $R = \left(q\eta + 2\right)/3.$
Global method	**Exp-Global** $S = \ln\frac{3}{2} + q\eta\ln\frac{4}{3}$	**DblExp-Global** $P = 2\lambda\left(1 - \ln 2\right) + q^2\eta\left(1 - q\eta\right)\left(\ln 3 - 1\right),$ $Q = \lambda - 2q^2\eta\left(1 - \ln\frac{81}{32} + 2q\eta\ \ln\frac{9}{8}\right),$ $R = q\eta + 2\left(1 - q\eta\right)\ln\left(3/2\right).$

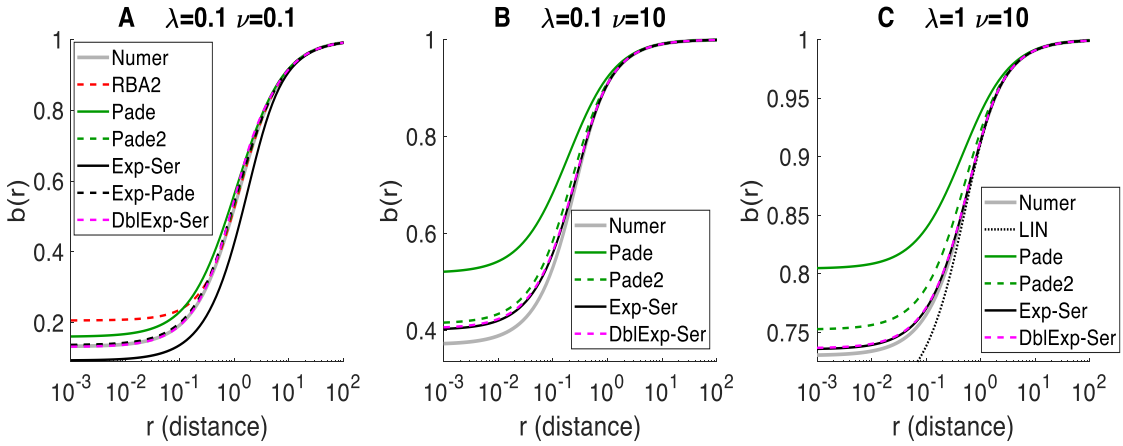

Figure 2.1 Equilibrium nanodomain buffer concentration approximations obtained using the series interpolation method: 1st-order Padé (*green*), 2nd order Padé (Padé2, *dashed green*), Exp-Ser (*black*), Exp-Padé, (*dashed black*), and DblExp-Ser (*dashed magenta*). Also shown for comparison is RBA2 (A, *dashed red*) and Linear approximation (C, *dotted black*). All panels show free dimensionless buffer concentration as a function of distance from the Ca^{2+} channel, for three distinct choices of model parameters λ and ν, as indicated in the panel title, with η =1. *Grey curves* show the accurate numerical solution. In (A), DblExp-Ser, Padé2 and Exp-Padé are indistinguishable from the numerical solution on this scale. Note that Exp-Padé does not yield a solution for $\nu > \eta$ =1 (B, C). In (A), DblExp-Ser curve shows the real part of Equation 2.26.

Figure 2.1 compares the three approximants described above (Exp-Ser, DblExp-Ser, Exp-Padé) with the previously developed Padé series interpolants of two lowest orders, as well as RBA2 (Figure 2.1A), and LIN (Figure 2.1C). The accurate numerical solution is shown as a gray curve. For the parameters in Figure 2.1A (λ=ν=0.1), Exp-Ser (*black curve*) isn't as accurate as other approximants, but the accuracy of Exp-Padé (*dashed black curve*) and DblExp-Ser (*dashed magenta curve*) is excellent, and comparable to that of Padé2 (*dashed green curve*); in fact, the three curves completely overlap with the numerical solution curve. This is despite the fact that α in DblExp-Ser expression is complex for λ=ν=0.1, so this is not an optimal parameter region for DblExp-Ser, and the real part of Equation 2.26 is used in this case. For larger values of λ and/or ν in Figures 2.2B (λ=0.1, ν=10) and 2.2*C* (λ=1, ν=10), approximants Exp-Ser and DblExp-Ser are more

accurate than Padé and even Padé2. These results suggest that these series interpolants may be superior to previously developed approximants in estimating Ca^{2+} nanodomains in a wide range of model parameters. Among previously developed approximants listed in Table 2.1, only RBA2 provides comparable accuracy, in the case $\lambda<1$, corresponding to parameters in Figure 2.1A (*dashed red curve*).

Comparing the results by eye for several combinations of model parameters is clearly insufficient to unveil the parameter-sensitivity of approximant accuracy; in fact, the difference between several approximants is almost impossible to tell from Figure 2.1. Therefore, following prior work (19, 33, 34), we explore parameter dependence of the absolute deviation between the given approximation b_{approx} and the accurate numerical solution, b_{numer}:

$$\left\| b_{approx} - b_{numer} \right\| = \frac{1}{N} \sum_{n=1}^{N} \left| b_{approx}(r_n) - b_{numer}(r_n) \right|, \qquad r_n = 10^{-3+5n/N},\ n = 1, 2, \ldots N. \tag{2.28}$$

The deviations are computed on a set of N=100 points spanning 5 orders of magnitude of distance r, from 10^{-3} to 10^{2}. Since we use exponentially spaced points, this norm is equivalent to an L^1 norm weighted by $1/r$, and therefore it requires a short-range cut-off (we pick $r \geq 10^{-3}$). The higher weight at small r is justified by the fact that the short distance range is of greater interest, physically. Figure 2.1 indicates that the chosen range of r is sufficient to capture the qualitative behavior of solutions for a wide range of parameter values. We checked that none of the conclusions are changed qualitatively by choosing an L^∞ norm instead.

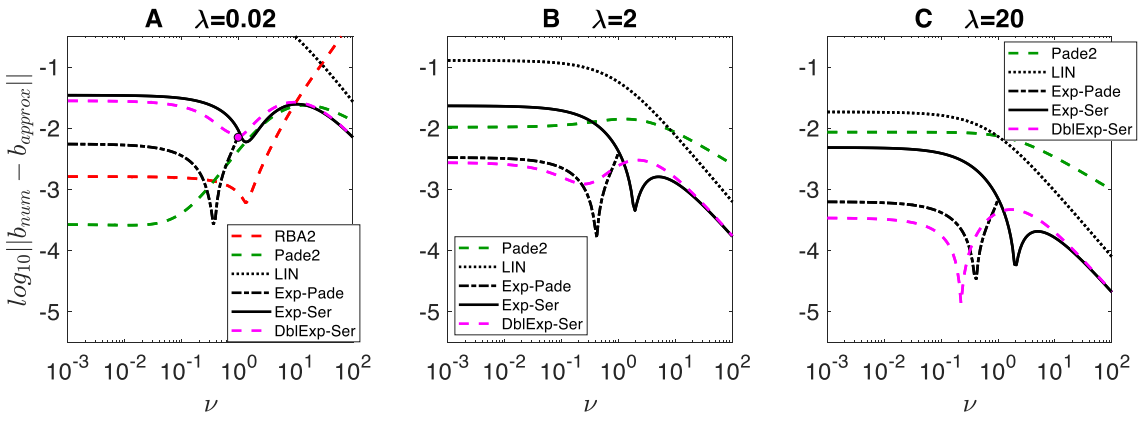

Figure 2.2 Accuracy comparison of equilibrium free buffer concentration approximations obtained by the series interpolation method: Exp-Ser (*black curves*), Exp-Padé (*dashed black curves*), DblExp-Ser (*dashed magenta curves*), and Padé2 (*dashed green curves*). Also shown is LIN (*dotted black curves*) and RBA2 (*red dashed curve*). RBA2 is only shown in A, since it requires λ<1. All curves show the error norm given by Equation 2.28 , on base-10 logarithmic scale, as a function of model parameter ν ranging from 10^{-3} to 10^2, for three distinct choices of λ: λ=0.02 (A), λ=2 (B), and λ=20 (C), with η =1. Since Exp-Padé only yields a solution for $\nu < \eta$ =1, the corresponding curves terminate at ν=1. *Magenta circle* in (*A*) indicates the value of ν below which the exponent parameter α of DblExp-Ser becomes imaginary (this occurs for λ<1.8). For smaller value of ν, the *magenta* curve in *A* corresponds to the real part of Equation 2.26.

The parameter dependence of this error norm is shown in Figure 2.2, as the value of ν is systematically varied from 10^{-2} to 10^2, for three distinct values of λ. Each curve shows the error measure given by Equation 2.28 for the corresponding approximation. For the sake of comparison, also shown are the error of the 2nd order Padé interpolant (Padé2, *dashed green curves*), the linear approximant (LIN, *dashed black curves*), and RBA2 (*dashed red curve*, Figure 2.2A only). For smaller values of λ (Figure 2.2A), Padé2 and RBA2 are still the superior approximation methods, but with increasing λ, the exponential series interpolation approximants outperform all approximants in Table 2.1 in estimating free buffer concentration. Thus, the choice of the optimal approximation method depends on the particular combination of model parameter values.

2.3.3 Variational Approach

We now consider a completely different method of approximating solutions, based on a variational approach. As was rigorously proven in (48) (see Appendix 4 therein), the solution to Equation 2.14 represents a unique minimizer of the following functional, in an appropriate function space:

$$F\left[b\right]=\int_{\mathbb{R}^3}\left[\frac{\lambda}{2}\left|\nabla b\right|^2+V\left(b,\mathbf{r}\right)-V\left(b_{RBA}\left(\mathbf{r}\right),\mathbf{r}\right)\right]d^3r \tag{2.29}$$

where $V(b, \mathbf{r})$ is defined by

$$V\left(b,\mathbf{r}\right)=-\eta b+\left(\frac{1}{|\mathbf{r}|}+\eta-\nu\right)\frac{b^2}{2}+\frac{\nu b^3}{3}, \tag{2.30}$$

and $b_{\mathrm{RBA}}(\mathbf{r})$ is the 1st-order RBA approximants given in Table 2.1, which solves Equation 2.14 when λ=0. Subtraction of $V(b_{\mathrm{RBA}}(\mathbf{r}), \mathbf{r})$ in Equation 2.29 is necessary to ensure boundedness of $F[b]$. Considering perturbations $b\rightarrow b+\varepsilon\phi,$ where ϕ is a smooth function with compact support $\left(\phi\in C_c^{\infty}\left(\mathbb{R}^3\right)\right)$, and denoting $V'\left(b,\mathbf{r}\right)$ the 1st partial derivatives with respect to b, the variational derivative (the Gâteaux derivative) of $F[b]$ in the direction of ϕ is

$$
\begin{aligned}
D_\phi F\left[b\right] &= \lim_{\varepsilon\to\infty}\frac{F\left[b+\varepsilon\phi\right]-F\left[b\right]}{\varepsilon} \\
&= \int_{\mathbb{R}^3}\left\{\lambda\nabla b\cdot\nabla\phi + V'\left(b,\mathbf{r}\right)\phi\right\}d^3r \\
&= \int_{\mathbb{R}^3}\left\{\lambda\nabla b\cdot\nabla\phi + \left[\left(b-1\right)\left(\nu b+\eta\right)+\frac{b}{|\mathbf{r}|}\right]\phi\right\}d^3r.
\end{aligned}
\tag{2.31}
$$

Therefore, setting

$$
D_\phi F\left[b\right] = 0 \;\; for \;\; \forall\phi\in C_c^\infty\left(\mathbb{R}^3\right), \tag{2.32}
$$

formally yields the weak (47) form of Equation 2.14. As is proved in (48) (see Appendix 4 therein), the minimizer of $F[b]$ is unique and radially symmetric. Therefore, we seek an *ansatz* of the form $b(r;\alpha_k)$, and consider perturbations with respect to the *ansatz* parameters α_k, i.e., we take $\phi = \partial b\left(r;\alpha_k\right)/\partial\alpha_k$. Performing integration by parts in the derivative term transforms Equations 2.31-2.32 to

$$
\frac{\partial F\left[b\left(r;\alpha_k\right)\right]}{\partial\alpha_k} = 4\pi\int_0^\infty E\left[b\left(r;\alpha_k\right)\right]\frac{\partial b}{\partial\alpha_k}r^2dr = 0, \tag{2.33}
$$

where $E[b]$ is defined in Equation 2.18. For the *ansätze* given by Equations 2.25-2.27, this integral may be computed in closed form, allowing to obtain the optimal values of parameters α_k by differentiation. For the lowest-order exponential *ansatz* (Equation 2.25), considering $b(r;\alpha)$ with one free parameter in Equation 2.33 leads to a quadratic equation for α with a unique positive real root, as given in Table 2.2. The corresponding

approximant will be referred to as Exp-Var (see Table 2.2). Note the similarity in the expression for α, as compared to the series interpolant method result in Table 2.2.

For the more complicated case of a double exponential *ansatz* (Equation 2.26), Equation 2.33 leads to a cubic rather than a quadratic equation for α, analogously to the series interpolation method; this cubic is shown in Table 2.2, and its closed-form solution is given in Appendix A. This cubic has a single real positive real root for a wide range of model parameters $\{\lambda,\ \nu,\ \eta\}$, and we refer to the corresponding approximant as DblExp-Var. However, just like in the case of DblExp-Ser, α becomes complex when both λ and ν are sufficiently small. In this parameter regime, the real part of Equation 2.26 still provides an accurate approximant. The performance of Exp-Var and DblExp-Var approximants will be investigated below, after considering our final approximation method.

2.3.4 Global Method: Modification of the Variational Approach

Given that Equations 2.25-2.26 represent narrow classes of functions that cannot provide a true minimum of $F[b]$, it may be useful to consider modifications of Equation 2.33 that allow to achieve a lower value of our chosen error norm given by Equation 2.28. One such modification is to replace the Jacobian factor r^2 in Equation 2.33 with the first power of r, increasing the contribution of small distances in this integral, and thereby potentially reducing the error at short range:

$$\int_0^\infty E\Big[b\big(r;\alpha\big)\Big]\frac{\partial b}{\partial \alpha} r\, dr = 0 \tag{2.34}$$

We refer to this method of setting approximant parameter values as the *Global* method or modified variational method. Equation 2.34 can be rigorously obtained from the variational derivative given by Equations 2.31-2.32, but this time applied to perturbations ϕ of form

$$\phi(r) = \frac{1}{r}\frac{\partial b(r;\alpha)}{\partial \alpha} \tag{2.35}$$

We note that for the *ansätze* in Equations 2.25-2.26, this perturbation remains finite as $r \to 0$. Numerical results show that this modification *does* lead to noticeable improvement of the resulting approximants close to the channel location, for some combinations of model parameters. In fact, for some parameter regimes this method clearly outperforms the series interpolation and the variational approaches with respect to the weighted L_1 error measure given by Equation 2.28.

For the lowest order exponential *ansatz* (Equation 2.25), after replacing $b(r;\alpha)$ in Equation 2.34 with Equation 2.25, one obtains a quadratic equation for α with a single positive real root given in Table 2.2; we refer to the corresponding approximant as Exp-Global. Just as in the case of the series intepolant method and the variational method, applying this method to the double exponential *ansatz* (Equation 2.26) leads to a cubic equation for parameter α, given in Table 2.2. We verified that this cubic has a single real positive real root for a wide range of model parameters $\{\lambda, \nu, \eta\}$, and we refer to the corresponding approximant as DblExp-Global. However, like in the case of DblExp-Ser and DblExp-Var approximants, parameter α becomes imaginary when both λ and ν are sufficiently small; in that case, the real part of Equation 2.26 will be used.

We note that a more straightforward approach of minimizing a weighted L^2 norm of $E[b]$ also leads to a closed-form solution in the case of a single-exponential *ansatz*, but the resulting approximant does not perform significantly better than the ones we present above, and its parameter α is given by solution to a more complicated 4th order polynomial equation.

2.3.5 Accuracy of the Variational and Global Approximants

Figure 2.3 compares all variational and global approximants described above (Exp-Var, DblExp-Var, Exp-Global and DblExp-Global) with Padé2 and the accurate numerical solution, using the same combination of model parameters as in Figure 2.1. It shows that in some cases (Figure 2.3B, C) the global approximations are more accurate than Padé2 and other series interpolants (cf. Figure 2.3B, C). Further, in Figures 2.3B and 2.3C, global approximants perform better than the corresponding variational approximants, and the differences between global methods and numerical results are barely noticeable. In contrast, Figure 2.3A illustrates that for ν=λ=0.1, none of the variational and global approximants are as accurate as Padé2, suggesting that the series interpolation methods may be superior for small values of ν and λ. We conclude the variational method and the global method can be great improvements compared with the series interpolation method in some, but not all, parameter regimes.

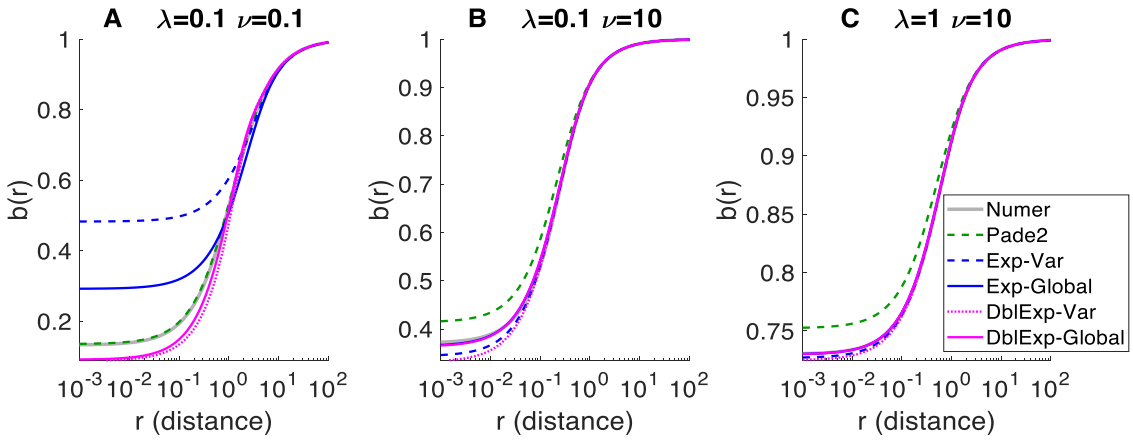

Figure 2.3 Comparison of equilibrium buffer concentration approximants obtained using the variational and the modified variational (global) methods: Exp-Var (*dashed blue curves*), DblExp-Var (*dotted magenta curves*), Exp-Global (*blue curves*), and DblExp-Global (*magenta curves*). Padé2 is also shown for comparison (*dashed green curves*). All panels show the free dimensionless buffer concentration as a function of distance from the Ca^{2+} channel, for three distinct choices of model parameters λ and ν, with η=1. *Grey curves* show the accurate numerical solution. In (A), the real part of DblExp-Var and DblExp-Global is shown. In (B) and (C), the curves for Exp-Global and DblExp-Global overlap the numerical solution.

Figure 2.4 shows a more systematic comparison to reveal the accuracy of the approximants obtained using the variational and the global methods in more detail. As in Figure 2.2, the value of ν is systematically varied from 10^{-2} to 10^{2}, for three different fixed values of dimensionless buffer diffusivity parameter λ. Each curve shows the average absolute error in buffer concentration approximation, as given by Equation 2.28. The error of the series interpolant DblExp-Ser is also shown for comparison in all panels, while Figure 2.4A also shows the accuracy of RBA2 and Padé2. For small values of ν and λ (Figure 2.4A), RBA2, Padé2, and even DblExp-Ser outperform the global approximants. However, as one increases the values of ν and λ, global approaches are starting to show their advantage. For most parameter regimes, approximations obtained using the modified variational (i.e., *global*) method are more accurate than the corresponding approximations

obtained using the unmodified variational method. For example, in all panels of Figure 2.4, Exp-Global (*blue curves*) is superior to Exp-Var (*dashed blue curves*).

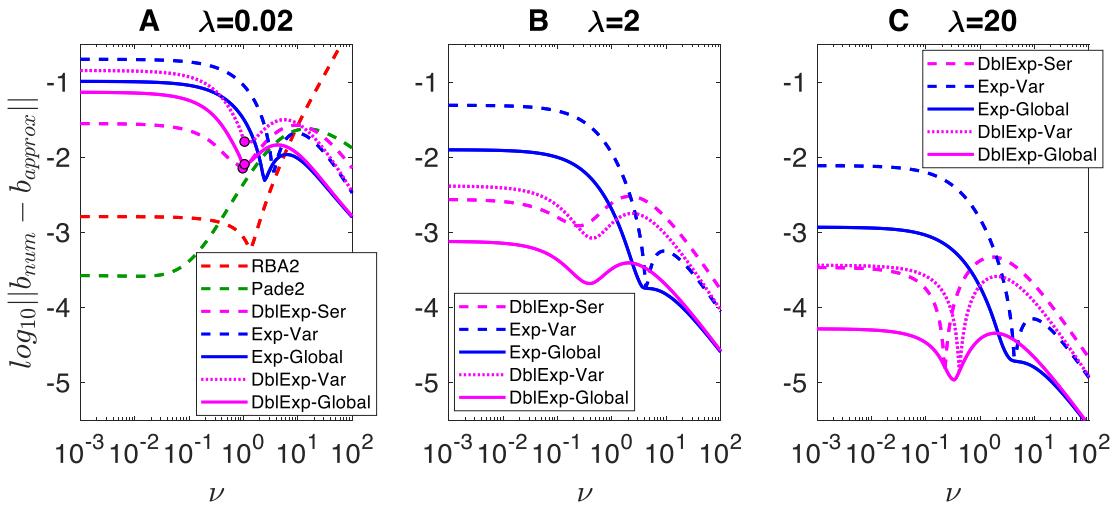

Figure 2.4 Accuracy comparison of equilibrium nanodomain free buffer concentration approximations obtained by the variational and modified variational (global) methods: Exp-Var (*dashed blue curves*), DblExp-Var (*dotted magenta curves*), Exp-Global (*blue curves*), and DblExp-Global (*magenta curves*). For comparison, also shown is the error of DblExp-Ser (*dashed magenta curves*), and (A) shows the errors of RBA2 (*dashed red curves*) and Padé2 (*dashed green curves*). All panels show the average absolute deviation of free dimensionless buffer concentration (Equation 2.28), on log-10 scale, as a function of buffer strength parameter ν ranging from 10^{-3} to 10^{2}, for three distinct choices of fixed model parameter λ: λ=0.02 (A), λ=2 (B), and λ=20 (C), with η=1. *Magenta circles* in (*A*) mark values of ν below which parameter α becomes imaginary for the corresponding DblExp method. For these smaller value of ν, the magenta curves in (*A*) represent the accuracy of buffer concentration given by the real part of Equation 2.26.

We note that the 2nd term in the DblExp approximants reflects the 2nd term in the long-range asymptotic series, which scales as $q^3=1/(\eta+\nu)^3$, therefore the double-exponential and the mono-exponential *ansätze* become equivalent when q is sufficiently small, corresponding to large values of buffer strength parameter ν. This behavior of accuracy as $\nu\to\infty$ is apparent in Figures 2.2 and 2.4.

2.3.6 Accuracy in Approximating Ca^{2+} Concentration

As noted above, Ca^{2+} concentration is uniquely determined from the equilibrium buffer concentration through the Ca conservation law, Equation 2.15. Nevertheless, it is useful to look separately at the accuracy of the Ca^{2+} estimation by the methods we present. Close to the channel location Ca^{2+} concentration is dominated by the unbounded point source term, $1/r$, and therefore we will use a logarithmic error measure when comparing Ca^{2+} concentration approximations (19, 33, 34):

$$\left\| c_{approx} - c_{numer} \right\| = \frac{1}{N} \sum_{n=1}^{N} \left| \ln c_{approx}\left(r_n\right) - \ln c_{numer}\left(r_n\right) \right| \tag{2.36}$$

This sum extends over the same logarithmically spaced points that were used for the buffer error measure given by Equation 2.28, namely a set of 100 points spanning 5 orders of magnitude of distance.

Figure 2.5 plots this Ca^{2+} error measure for the optimal approximations that achieve the greatest accuracy over the wide range of model parameters λ and ν. Because of the difference between the buffer and the Ca^{2+} error measures (cf. Equation 2.28 vs. Equation 2.36), the accuracy profile of different Ca^{2+} concentration approximants shown in Figure 2.5 doesn't match perfectly the accuracy of the corresponding free buffer approximants shown in Figures 2.2 and 2.4, despite the one-to-one relationship between the Ca^{2+} concentration and free buffer. As explained above, the relative error in Ca^{2+} concentration estimation is particularly sensitive to the accuracy of the method at intermediate distances, rather than its accuracy in the vicinity of the channel, as is the case for the free buffer error measure (19, 34). Note in particular that the DblExp-Var or DblExp-Global yield the most

accurate Ca^{2+} approximations for $\lambda \geq 1$ (see Figures 2.5B, C), contrary to the error in buffer estimation, which is minimized by the Exp-Global and DblExp-Global approximants (cf. Figures 2.4B, C). However, for small values of λ, RBA2 and Padé2 are the best methods for estimating both Ca^{2+} and buffer concentration (Figures 2.4A, 2.5A).

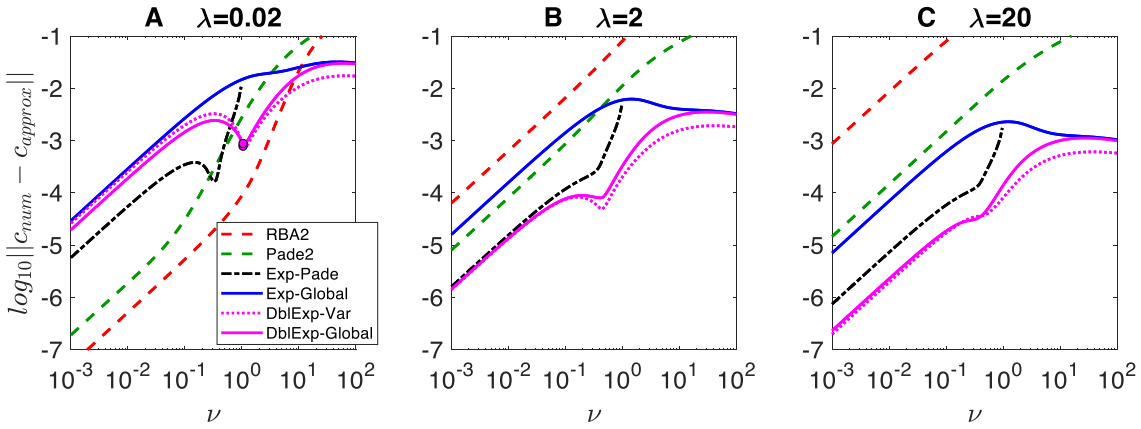

Figure 2.5 Accuracy comparison of equilibrium nanodomain Ca^{2+} concentration estimation by select optimal approximations (methods with smallest error): RBA2 (*red dashed curves*), Padé2 (*dashed green curves*), Exp-Padé (*dot-dashed black curves*), Exp-Global (*blue curves*), DblExp-Global (*magenta curves*), and DblExp-Var (*dotted magenta curves*). All panels show average absolute deviation of free dimensionless Ca^{2+} concentration (Equation 2.36), on base-10 logarithmic scale, as a function of buffering strength parameter ν ranging from 10^{-2} to 10^{2}, for three distinct choices of diffusivity parameter λ: λ=0.02 (A), λ=2 (B), and λ=20 (C), with η=1. Curves for Exp-Padé (*dashed black curves*) terminate at ν=1.

2.3.7 Summary of Results and Choice of Optimal Method

Figure 2.6 summarizes all results presented in Figures 2.1-2.5, marking the best approximants and their errors for a wide range of buffer mobility λ and buffering strength ν varying over 5 orders of magnitude. It shows that the methods we presented significantly improve the accuracy of approximation for a wide range of model parameters, and especially those corresponding to larger values of buffer mobility λ and buffering strength ν. In fact, these methods outperform all previously developed approximants with the

exception of the 2nd-order RBA and 2nd-order Padé (19, 34), the two methods which are still superior in particular regions of parameter space corresponding to small buffer mobility λ and small-to-moderate buffering strength ν.

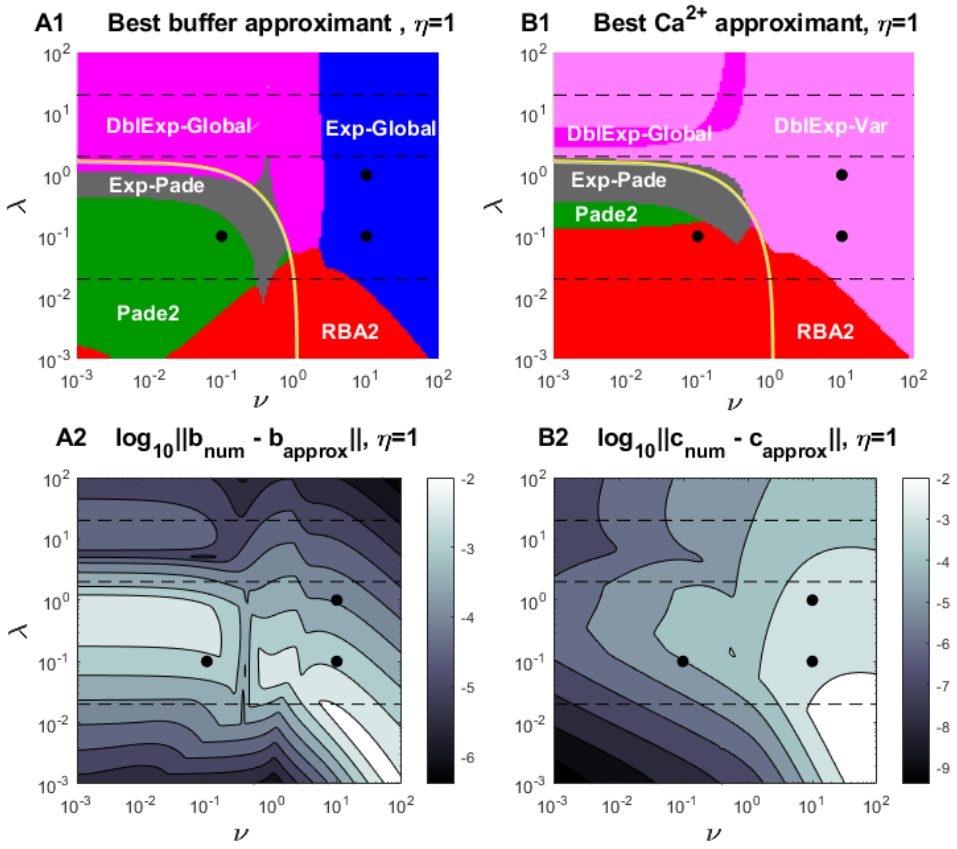

Figure 2.6 Comparison of parameter regions where a given approximant outperforms the rest in estimating (A1) free buffer and (B1) Ca^{2+} concentration in the (ν, λ) parameter plane, according to the error measures given by Equations 2.28 and 2.36. In all panels, η=1. Colors indicate parameter region of best performance for each approximant: Padé2 (*green*), RBA2 (*red*), Exp-Padé (*gray*), DblExp-Var (*pink*), DblExp-Global (*magenta*), Exp-Global (*blue*). Black circles correspond to parameter values in Figures 2.1, 2.3, and dashed lines corresponds to the parameter sweep curves in Figures 2.2, 2.4-2.5. Thin light semi-circular curves indicate the boundaries inside of which the exponent parameter α in the DblExp-Var and DblExp-Global methods becomes imaginary (α is always real outside of the region marked by these curves, for $\nu > 1$ and $\lambda > 1.8$). Lower panels show the smallest error in estimating buffer (A2) and Ca^{2+} (B2) concentrations achieved using the optimal approximants shown in top panels. The grayscales in A2 and B2 indicate the log-10 of error values given by Equations 2.28 and 2.36, respectively. Darker gray-level corresponds to better accuracy.

Figure 2.6A1, B1 can be used to design a simple algorithm for the selection of the optimal method. We find that such algorithm can be further simplified by using just three methods, Padé2, RBA2 and DblExp-Global, with only a minor sacrifice in accuracy. Below is the full sequence of steps allowing to achieve good accuracy in the entire parameter range that we explored, combined with the steps needed to obtain final results in physical units:

1) Compute all non-dimensional parameters (Equations 2.10, 2.12, 2.13).
2) Find the non-dimensional buffer concentration b using one of three methods:
    a) If $\lambda\nu < 0.1$ and $\lambda\eta < 0.03$, then use RBA2 (Table 2.1)
    b) Otherwise, use DblExp-Global, if its parameter α is real (Equations 2.26, A.1-A.3)
    c) Otherwise, use Padé2 (Table 2.1, Equations C.1, C.2)
3) Compute non-dimensional Ca^{2+} concentration c using the conservation law, Equation 2.15.
4) Convert concentrations to physical units: $[Ca^{2+}] = c\,K$, $[B] = bB_\infty$.

Here K denotes buffer's affinity, and B_∞ is the free buffer concentration far from the channel.

Figure 2.7 shows the accuracy of the approximants chosen according to this simplified algorithm remains within 1% even for this simplified approach, for a very wide range of λ and ν values, and two different values of η, namely η=1 and η=10. Note that the overall accuracy is increased at higher values of $\eta = c_\infty + 1/\delta_B^*$, which corresponds to higher background Ca^{2+} concentration and/or reduced mobility of the Ca^{2+}-bound buffer state. Results in Figures 2.6A1, B1 reveal that a somewhat better performance could be achieved if the buffer and Ca^{2+} concentration approximations are chosen independently for

a given set of parameter values, but this would lead to only a minor improvement. Apart from algorithm simplicity, choosing the same method for Ca^{2+} and buffer concentration estimates guarantees that the conservation law, Equation 2.15, is satisfied.

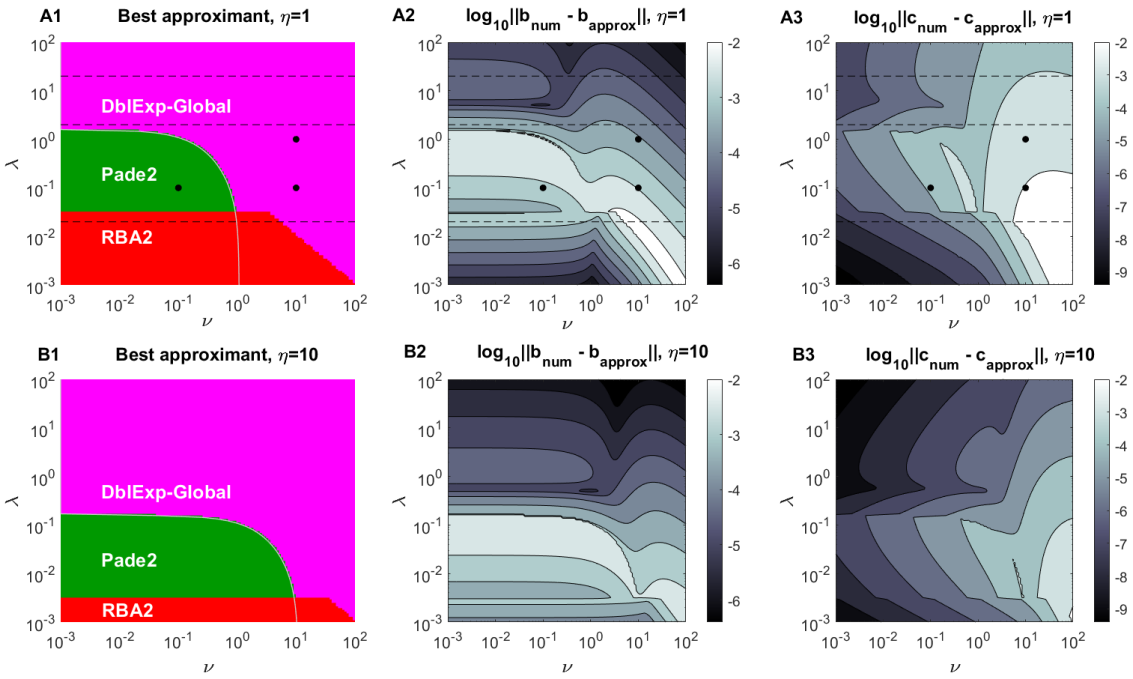

Figure 2.7 Simplified algorithm for choosing an optimal approximant among the subset Padé2, RBA2, and DblExp-Global, for two values of parameter η: η=1 (A1-A3), and η=10 (B1-B3). (A1, B1): the best method as a function of parameters ν and λ, chosen according to the algorithm described in the text. Colors indicate the parameter region for each approximant: Padé2 (*green*), RBA2 (*red*), and DblExp-Global (*magenta*). Black circles correspond to parameter values in Figures 2.1, 2.3, and dashed lines corresponds to the parameter sweep curves in Figures 2.2, 2.4, 2.5. Thin light semi-circular curves indicate the boundaries inside of which the exponent parameters α in the DblExp-Global approximant becomes imaginary. Lower panels show the smallest error in estimating buffer (A2, B2) and Ca^{2+} (B3, A3) concentrations achieved using the approximants chosen as indicated in A1 and B1. The grayscales in A2 and B2 indicate the log-10 of error values in Equations 2.28 and 2.36, respectively. The same grayscale is used for η=1 and η=10, for ease of comparison. Darker gray level corresponds to better accuracy.

CHAPTER 3

COMPLEX BUFFER CASE

3.1 Methods: Single-channel Ca^{2+} Nanodomain Equation

We start with the description of the Ca^{2+} binding and unbinding reactions for buffer molecules with two binding sites, which we will refer to as two-to-one buffers or complex buffers (33, 37, 40):

$$B \underset{k_1^-}{\overset{2[Ca^{2+}]k_1^+}{\rightleftharpoons}} B^* \underset{2k_2^-}{\overset{[Ca^{2+}]k_2^+}{\rightleftharpoons}} B^{**}. \tag{3.1}$$

Here B, B^* and B^{**} denote respectively the free, partially bound, and fully Ca^{2+}-bound states of the buffer, and $k_{1,2}^+$, $k_{1,2}^-$ are the Ca^{2+}-buffer binding/unbinding rates for each buffer state. The rest of the problem is formulated under the same assumptions considered in the case of a simple buffer, as described in Chapter 2. Namely, we will consider a semi-infinite domain bounded by a flat plane representing the cytoplasmic membrane, which contains one or more Ca^{2+} channels. Further, we assume zero flux boundary condition for Ca^{2+} and buffer on the flat plane, so the reflection symmetry allows to extend the domain to infinite space, while doubling the current strength, which places the Ca^{2+} current sources inside the domain (18, 19, 27). Denoting free Ca^{2+} concentration as C, and time differentiation as ∂_t, we arrive at the following reaction-diffusion system for the concentrations of all reactants (33):

$$\begin{cases} \partial_t C = D_C \nabla^2 C - R_1 - R_2 + 2\sum_{k=1}^{N_{Ca}} \sigma_k \delta(\mathbf{r} - \mathbf{r}_k), \\ \partial_t B = D_B \nabla^2 B - R_1, \\ \partial_t B^* = D_B^* \nabla^2 B^* + R_1 - R_2, \\ \partial_t B^{**} = D_B^{**} \nabla^2 B^{**} + R_2, \end{cases} \tag{3.2}$$

where the reaction terms are given by

$$\begin{cases} R_1 = 2k_1^+ C B - k_1^- B^*, \\ R_2 = k_2^+ C B^* - 2k_2^- B^{**}. \end{cases} \tag{3.3}$$

In Equation 3.2, the point channel-source strengths are $\sigma_k = I_{Ca,k}/(2F)$, where $I_{\mathrm{Ca,k}}$ are the amplitudes of individual open Ca^{2+} channels located at positions $\mathbf{r}_k$, F is the Faraday constant, and N_{Ca} is the number of Ca^{2+} channels. As in the simple-buffer case (19, 21, 34, 43, 44), there are two conservation laws for the total buffer and the total Ca^{2+} concentrations:

$$\partial_t \left(B + B^* + B^{**} \right) = \nabla^2 \left(D_B B + D_B^* B^* + D_B^{**} B^{**} \right), \tag{3.4}$$

$$\partial_t \left(C + B^* + 2B^{**} \right) = \nabla^2 \left(D_C C + D_B^* B^* + 2D_B^{**} B^{**} \right) + 2\sum_{k=1}^{N_{Ca}} \sigma_k \delta(\mathbf{r} - \mathbf{r}_k). \tag{3.5}$$

Since we are interested in equilibrium solutions, we obtain

$$\begin{cases} D_B \nabla^2 B \;\; = R_1, \\ D_B^{**} \nabla^2 B^{**} = -R_2, \\ \nabla^2 \left(D_B B + D_B^{*} B^{*} + D_B^{**} B^{**} \right) = 0, \\ \nabla^2 \left(D_C C + D_B^{*} B^{*} + 2 D_B^{**} B^{**} \right) = -2 \sum_{k=1}^{N_{Ca}} \sigma_k \delta(\mathbf{r} - \mathbf{r}_k). \end{cases} \tag{3.6}$$

Following prior work (33), here we assume that buffer diffusivity does not change when binding Ca^{2+} ions, $D_B = D_B^{*} = D_B^{**}$ (this constraint is relaxed in the derivation of the RBA shown in Appendix F). In this case the two conservation laws in Equation 3.6 have the following solution (19, 21, 27, 33, 43, 44):

$$\begin{cases} B + B^{*} + B^{**} = B_T = const, \\ D_C C + D_B \left(B^{*} + 2B^{**} \right) = \dfrac{1}{2\pi} \displaystyle\sum_{k=1}^{N} \frac{\sigma_k}{|\,\mathbf{r} - \mathbf{r}_k\,|} + C_T, \end{cases} \tag{3.7}$$

where constants B_T and C_T are related to the total (bound plus free) buffer and Ca^{2+} concentrations respectively, infinitely far from channel:

$$\begin{cases} B_T = B_\infty + B_\infty^{*} + B_\infty^{**}, \\ C_T = D_C C_\infty + D_B \left(B_\infty^{*} + 2B_\infty^{**} \right). \end{cases} \tag{3.8}$$

Here X_∞ denote the concentrations of reactants X infinitely far from the channel, where reactions given by Equation 3.3 are at equilibrium. Therefore, all background buffer state concentrations are uniquely determined by the background $[Ca^{2+}]$, C_∞, through equilibrium relationships

$$\begin{cases} 2C_\infty B_\infty = K_1 B_\infty^*, \\ C_\infty B_\infty^* = 2K_2 B_\infty^{**}, \end{cases} \tag{3.9}$$

where $K_{1,2}$ are the affinities of the two reactions in Equations 3.1, 3.3, given by $K_1 \equiv k_1^- / k_1^+$ and $K_2 \equiv k_2^- / k_2^+$.

We now restrict to the case of a single Ca^{2+} channel of source strength $\sigma = I_{Ca}/(2F)$ at the origin, and look for spherically symmetric solutions, which turns Equation 3.6 into a system of ODEs, with the spherically symmetric Laplacian given in terms of the distance from the Ca^{2+} channel, $r=|\mathbf{r}|$:

$$\nabla^2 = \frac{1}{r^2}\frac{d}{dr}\left(r^2 \frac{d}{dr} \right). \tag{3.10}$$

We now non-dimensionalize the problem using an approach analogous to the one we used for a simple buffer in Chapter 2. As we mentioned earlier, this is a slightly modified version of the non-dimensionalization introduced by Smith et al (19) and also used in (33, 34). Namely, we normalize Ca^{2+} and buffer concentrations by the affinity of the 2nd binding step and the background buffer concentration, respectively:

$$c = \frac{C}{K_2},\ b = \frac{B}{B_\infty},\ b^* = \frac{B^*}{B_\infty},\ b^{**} = \frac{B^{**}}{B_\infty}. \tag{3.11}$$

We also re-scale the spatial coordinate ($r/L \rightarrow r$) using the scale parameter that depends on the strength of the Ca^{2+} current,

$$L = \sigma / \left(2\pi K_2 D_C \right). \tag{3.12}$$

This transforms Equations 3.6, 3.7 into the form

$$\begin{cases} \lambda_1 \nabla^2 b \;\; = 2\varepsilon c b - b^*, \\ \lambda_2 \nabla^2 b^{**} = -c\, b^* + 2 b^{**}, \\ b + b^* + b^{**} = b_T, \\ c + \dfrac{\nu_2}{2}\left(b^* + 2 b^{**} \right) = \dfrac{1}{r} + c_T, \end{cases} \tag{3.13}$$

where b_T and c_T are the non-dimensional versions of integration constants given by Equation 3.8, related to total buffer and Ca^{2+} concentrations infinitely far from the channel (note that in our non-dimensionalization b_∞=1):

$$\begin{cases} b_T = 1 + b_\infty^* + b_\infty^{**}, \\ c_T = c_\infty + \dfrac{\nu_2}{2}\left(b_\infty^* + 2 b_\infty^{**} \right), \end{cases} \tag{3.14}$$

with dimensionless parameters

$$\lambda_{1,2} = \frac{D_B}{L^2 k_{1,2}^-}, \;\; \nu_{1,2} = \frac{2 B_\infty D_B}{K_{1,2} \; D_C}. \tag{3.15}$$

Along with c_∞, parameters $\lambda_{1,2}$ and $\nu_{1,2}$ completely specify the model system. Here $\lambda_{1,2}$ are the dimensionless mobilities of the two buffer states, which depend on buffering

kinetics and Ca^{2+} current amplitude through the length scale L (Equation 3.12). They quantify the ratio between the rate of diffusion and the rate of Ca^{2+} influx and binding. Parameters $\nu_{1,2}$ quantify the overall buffering strength, and equal the product of the relative buffer mobility, D_B / D_C, and the two quantities characterizing buffering capacity at rest, $2B_\infty / K_{1,2}$. For the sake of simplicity, we will also use the following cooperativity parameters, which characterize the difference between the affinities and kinetics of the buffer's two distinct Ca^{2+}-binding sites:

$$\varepsilon = \frac{\nu_1}{\nu_2} = \frac{K_2}{K_1},\ \gamma = \frac{\lambda_1}{\lambda_2} = \frac{k_2^-}{k_1^-}. \tag{3.16}$$

In the case of calretinin and calmodulin, the binding properties have been experimentally estimated (37, 41), and the corresponding values of cooperativity parameters are given in Table 3.1. These two Ca^{2+} buffer-sensors are characterized by highly cooperative Ca^{2+} binding, with $\varepsilon << 1$.

In the results shown below, we will use the cooeprativity parameters given by Equation 3.16 to replace some of the four parameter given by Equation 3.15. Namely, we will specify our model using either $\{\lambda_2, \nu_2, \varepsilon, \gamma\}$ or $\{\lambda_1, \lambda_2, \varepsilon, q\}$, where parameter q is anlogous to the parameter we introduced in the simple buffer case, namely $q=1/(1+\nu_1)$.

We now restrict our analysis to the case of zero background Ca^{2+} concentration, relegating the more general case $c_\infty \neq 0$ to Appendix E. With this simplification, $c_\infty = c_T = 0$ and $b_\infty = b_T = 1$, therefore Equation 3.13 becomes

$$\begin{cases} \lambda_1 \nabla^2 b &= 2\varepsilon c b - b^*, \\ \lambda_2 \nabla^2 b^{**} &= -c\, b^* + 2 b^{**}, \\ b + b^* + b^{**} &= 1, \\ c + \dfrac{\nu_2}{2}\left(b^* + 2 b^{**}\right) &= \dfrac{1}{r}. \end{cases} \tag{3.17}$$

Table 3.1 Ca^{2+} Binding Properties of Strongly Cooperative Buffers Calretinin (CaR) and Calmodulin (CaM), as Measured by Faas et al (37, 41). Each CR molecule contains 5 binding sites, consisting of two identical cooperative pairs of Ca^{2+}-binding sites and one independent non-cooperative site. CaM molecule consists of two independent domains (lobes), each binding two Ca^{2+} ions in a cooperative manner. Note the very high rate of the 2nd Ca^{2+} binding rate to the N-lobe of CaM, which is therefore extremely diffusion-limited. Values of λ_2 and ν_2 are calculated for Ca^{2+} current strength of I_{Ca}=0.4 pA, and total buffer concentrations of B_T=100 μM.

Parameter	k_1^+	k_2^+	K_1	K_2	$\varepsilon = \frac{K_2}{K_1}$	$\gamma = \frac{k_2^-}{k_1^-}$	λ_2	ν_2
Units	$(\mu M\ ms)^{-1}$	$(\mu M\ ms)^{-1}$	μM	μM				
CaR coop. sites	0.0018	0.31	28	0.068	$2.4\cdot10^{-3}$	0.42	$1.6\cdot10^{-3}$	294
CaR Non-coop. site	0.0073	--	36	--	--	--	--	
CaM (N-lobe)	0.77	32	193	0.788	$4\cdot10^{-3}$	0.17	$1.8\cdot10^{-4}$	25.4
CaM (C-lobe)	0.084	0.025	27.8	0.264	$9.5\cdot10^{-3}$	$2.85\cdot10^{-3}$	$7.8\cdot10^{-2}$	75.8

As in the simple buffer case, Equation 3.17 is challenging to analyze since it represents a non-linear and singular problem on an infinite domain. Further, most stationary approximations developed for the case of simple buffer cannot be extended to complex buffers (19, 33). As mentioned above, RBA is the only approximant that has been successfully extended to the case of complex buffer (33). RBA assumes that the reaction

is at equilibrium on the entire domain. In Appendix F we derive RBA using the new non-dimensionalization considered in this work, slightly generalizing the expressions in (33). As was found before for the case of simple buffer, RBA approximates the true solution very well within the parameter regime $\lambda_{1,2}<<1$ (19). However, for complex buffer, this parameter regime has a complex interplay with the cooperativity condition $\varepsilon<<1$. For example, the accuracy in buffer concentration estimation is significantly reduced with increasing Ca^{2+} binding cooperativity, corresponding to decreasing ε. However, reducing the unbinding rate ratio γ along with ε partially rescues RBA accuracy (33). This high sensitivity of RBA accuracy to buffer parameters calls for the development of other approximants. In the results shown below, the accuracy of newly developed approximants will be compared and contrasted with that of the RBA.

3.2 Results

3.2.1 Equilibrium Ca^{2+} Nanodomain: Power Series Interpolation Method

We begin by presenting the power series interpolation method developed in Chapter 2 for the case of simple buffers with one-to-one Ca^{2+} binding stoichiometry (34), which we will now generalize to the case of Ca^{2+} buffers with two binding sites. This method involves finding simple *ansätze* that interpolate between the solution's Taylor series in powers of distance from the channel location, *r*, and the asymptotic power series expansion of the solution in terms of the reciprocal distance from the channel location, $x=1/r$. We will refer to these two series as the short-range (low-*r*) and long-range (high-*r*) series.

We start with the non-dimensionalized form of the system for complex buffer, Equation 3.17, and make a substitution $U=(1-b)/\varepsilon$, and $V=b^{**}/\varepsilon$ to slightly simplify

the system. Eliminating the partially-bound buffer concentration variable using the buffer conservation law $b^* = 1 - b - b^{**} = \varepsilon(U - V)$, Equation 3.17 is transformed to

$$\begin{cases} \lambda_1 \nabla^2 U = 2c(\varepsilon U - 1) + U - V, \\ \lambda_2 \nabla^2 V = c(V - U) + 2V, \\ c + \dfrac{\nu_1}{2}(U + V) = \dfrac{1}{r}. \end{cases} \tag{3.18}$$

Next, we eliminate the Ca^{2+} concentration c using the Ca^{2+} conservation law in the system above to obtain

$$\begin{cases} \lambda_1 \nabla^2 U = 2\left[\dfrac{1}{r} - \dfrac{\nu_1}{2}\left(U + V\right)\right]\left(\varepsilon U - 1\right) + U - V, \\ \lambda_2 \nabla^2 V = \left[\dfrac{1}{r} - \dfrac{\nu_1}{2}\left(U + V\right)\right]\left(V - U\right) + 2V. \end{cases} \tag{3.19}$$

This system has only a regular singularity at r =0 and does have a solution analytic at r =0, representing the physical nanodomain solution that we are seeking. Using a formal series expansion similar to the Frobenius method we find the following Taylor series expansions in r for both U and V:

$$\begin{cases} U(r) = U_0 + \dfrac{\varepsilon U_0 - 1}{\lambda_1} r + \dfrac{(\varepsilon U_0 - 1)\left[2\varepsilon - \lambda_1 \nu_1 (U_0 + V_0)\right] + \lambda_1 (U_0 - V_0)}{6\lambda_1^2} r^2 + O(r^3), \\ V(r) = V_0 + \dfrac{V_0 - U_0}{2\lambda_2} r + \dfrac{2(1 - \varepsilon U_0) + \gamma(V_0 - U_0) + 4\lambda_1 V_0 + \lambda_1 \nu_1 (U_0^2 - V_0^2)}{12\lambda_1 \lambda_2} r^2 + O(r^3). \end{cases} \tag{3.20}$$

In above system U_0 and V_0 are related to the concentrations of free and fully bound buffer at channel location, r=0; these two values are finite and non-zero, but unknown *a priori*. Thus, U_0 and V_0 are important unknowns of the problem, to be determined by our

approximation procedure. Because U_0 and V_0 are unknown, the utility of Equation 3.20 is that it provides relationships between coefficients of these Taylor expansions. For example, denoting the 1st-order Taylor coefficients in Equation 3.20 as U_1 and V_1, we adjust the free parameters of each approximant considered further below by imposing the constraints $U_1=(\varepsilon U_0-1)/\lambda_1$ and $V_1=(V_0-U_0)/(2\lambda_2)$.

In order to obtain the long-range asymptotic series expansion of the solution, we make a coordinate mapping $x \equiv 1/r$, transforming Equation 3.19 to the form

$$\begin{cases} \lambda_1 x^4 U_{xx} = 2\left(x - \dfrac{\nu_1}{2}(U+V) \right)(\varepsilon U - 1) + U - V, \\ \lambda_2 x^4 V_{xx} = \left(x - \dfrac{\nu_1}{2}(U+V) \right)(V-U) + 2V. \end{cases} \tag{3.21}$$

This system has a unique asymptotic power series expansion near $x=0$ satisfying boundary conditions at $x\to 0^+$ (i.e., $r\to+\infty$), namely $U(x=0^+)=0$, $V(x=0^+)=0$. Up to terms of order x^3, this asymptotic series expansion can be obtained by simply equating the right-hand sides of Equation 3.21 to zero, which yields

$$\begin{cases} U(x) = 2qx + q^3\left[2 - 4\varepsilon - 1/q\right]x^2 + O(x^3), \\ V(x) = q^2x^2 - 2q^3\left[1 - q + \varepsilon\left(2q-1\right)\right]x^3 + O(x^4), \end{cases} \tag{3.22}$$

where we introduced the parameter $q = 1/(1+\nu_1)$ for the sake of simplicity. It is important to note that the leading term in the $V(x)$ long-range expansion is of order $O(x^2)$, in contrast to U. This is intuitive, since V represents the double-bound buffer state, which decays faster

than any other concentration measure as $x \to 0^+$ (i.e., $r \to +\infty$). Note however that this is not the case in the case of non-zero background $[Ca^{2+}]$; this more general case is considered in Appendix E. Parenthetically, we also note that the right-hand sides of Equation 3.21 contain all reaction terms, which RBA sets to zero, while the Laplacian gives rise to asymptotic terms of order $O(x^4)$; therefore up to the given order $O(x^3)$ this expansion agrees with the corresponding asymptotic expansion of the RBA, described in Appendix F.

We will now consider simple *ansätze* whose series expansions simultaneously match leading terms of the low-r (short-range) series and the low-x (long-range, high-r) series given by Equations 3.20, 3.22. Inspired by the simple buffer case, we seek *ansätze* for U and V that combine Padé approximants (rational functions) and exponential functions. Below we list these *ansätze* for U and V, along with the corresponding short-range and long-range series representations. Our approximations are based on pair-wise combinations of these U and V *ansätze*, as summarized in Table 3.2. By a slight abuse of notation, we use the same function name (U or V) whether it is expressed as a function of distance variable, r, or its reciprocal, x:

- Padé *ansatz* for U, containing one free parameter, A:

$$\begin{aligned} U(r) &= \frac{2q}{A+r} = \frac{2q}{A}\left[1 - \frac{r}{A} + \frac{r^2}{A^2} + O(r^3)\right], \\ U\left(x = \frac{1}{r}\right) &= \frac{2qx}{1+Ax} = 2q\left[x - Ax^2 + O(x^3)\right]. \end{aligned} \tag{3.23}$$

- Exponential *ansatz* for U, which depends on one free parameter, a:

$$U\left(r\right)=2q\frac{1-e^{-ar}}{r}=2qa-qa^2r+O(r^2),$$
$$U\left(x=\frac{1}{r}\right)\sim 2qx. \tag{3.24}$$

- Padé *ansatz* for V, which depends on two free parameters, b_1 and b_2:

$$V\left(r\right)=\frac{q^2}{r^2+b_1r+b_2}=q^2\left[\frac{1}{b_2}-\frac{b_1}{b_2^2}r+\frac{b_1^2-b_2}{b_2^3}r^2+O(r^3)\right],$$
$$V\left(x=\frac{1}{r}\right)=\frac{q^2x^2}{1+b_1x+b_2x^2}=q^2\left[x^2-b_1x^3+O(x^4)\right]. \tag{3.25}$$

- Exponential *ansatz* for V, which depends on one free parameter, s:

$$V\left(r\right)=q^2\frac{1-\exp\left(-sr\right)\left(1+sr\right)}{r^2}=q^2s^2\left(\frac{1}{2}-\frac{s}{3}r+\frac{s^2}{8}r^2+O\left(r^3\right)\right),$$
$$V\left(x=\frac{1}{r}\right)\sim q^2x^2. \tag{3.26}$$

Note that all of these *ansätze* are analytic at r=0, and that in the limit $r\rightarrow+\infty$ (x=1/r $\rightarrow 0^+$), they automatically match the leading non-zero term in the asymptotic series expansion of the solution given by Equation 3.22: $U(x)= 2qx + O(x^2)$, $V(x)=q^2x^2 + O(x^3)$. Additionally, all *ansätze* satisfy appropriate physical constraints. Namely, imposing conditions $A > 0$ and $a > 0$ guarantees that U is also positive and monotonically decreasing to $U(r\rightarrow+\infty) = 0$ for each *ansatz*, and therefore b=1 at infinity, since $U=(1-b)/\varepsilon$. This agrees with the observation that the free buffer concentration is increasing monotonically

from $b_0>0$ at the channel mouth to $b(r\to+\infty)=1$ infinitely far from the channel. Further, V is also always positive given positive parameters b_1, b_2, and s, and is monotonically decreasing to $V(r\to+\infty)=0$, therefore $b^{**}=0$ at infinity (recall that $V = b^{**}/\varepsilon$). This agrees with the fact that the fully bound buffer concentration is bounded and equals to zero infinitely far from the Ca^{2+} channel, where $[Ca^{2+}]=0$.

Table 3.2 List of All New Approximants for a Two-Site Buffer, Including the *Ansätze* for U and V and the Number of Terms in the Short-range and Long-range Solution Expansions (Equations 3.20, 3.22) Matched by Each V *Ansatz*. Note that all *ansätze* automatically match the term of order O(x) in U ($U \sim 2qx$) and the term of order O(x^2) in V ($V \sim q^2x^2$). The free parameter in the U *ansatz* is matched using terms of order O(r), while the free parameters in the V *ansatz* are matched using terms indicated in the last column.

Name	***U ansatz***	***V ansatz***	**Parameters**	***V* accuracy**
PadéA	$\frac{2q}{A+r}$	$\frac{q^2}{r^2+b_1r+b_2}$	N=3 (A, b_1, b_2)	O(r), O(x^3)
PadéB				O(r^2), O(x^2)
ExpPadéA	$2q\frac{1-e^{-ar}}{r}$	$\frac{q^2}{r^2+b_1r+b_2}$	N=3 (a, b_1, b_2)	O(r), O(x^3)
ExpPadéB				O(r^2), O(x^2)
PadéExp	$\frac{2q}{A+r}$	$q^2\frac{1-\exp(-sr)(1+sr)}{r^2}$	N=2 (A, s)	O(r), O(x^2)
ExpExp	$2q\frac{1-e^{-ar}}{r}$	$q^2\frac{1-\exp(-sr)(1+sr)}{r^2}$	N=2 (a, s)	O(r), O(x^2)

We match the free parameters in the above approximants following the same interpolation method as in the case of a simple (one-to-one) buffer (34). Namely, the unknowns are U_0 and V_0 in Equation 3.20, plus either two or three parameters

characterizing a particular approximant, as summarized in Table 3.2. We need 4 or 5 constraints to match these unknowns. The first 4 constraints are obtained by matching the first two terms (of order O(1) and O(r)) in the short-range Taylor series for both U and V, as given by Equation 3.20. For the 3-parameter approximants, the final 5th constraint is needed, which comes from matching one additional term in the short- or the long-range series of V, as specified in the last two columns of Table 3.2. One obtains an algebraic system of 4 or 5 equations for the *ansatz* parameters, which are readily solvable in closed form. Tables 3.3 and 3.4 show the exact expressions we obtain using this method for the free *ansatz* parameters in terms of the model parameters $\{\lambda_1, \lambda_2, q, \varepsilon\}$. Note that parameters b_2 and s are defined by solutions of cubic equations shown in the last column of Table 3.4, whose roots are given in closed form in Appendix D. Once b=1−εU and b^{**}=εV are determined using these approximants, the partially bound buffer concentration, b^*, and Ca^{2+} concentration, c, can then be determined from b and b^{**} through the conservation laws in Equation 3.17.

Table 3.3 *Ansätze* for the Free Buffer Variable U and Equations for Their Parameters as Functions of Non-dimensional Model Parameters q, ε, λ_1, and λ_2. Corresponding *Ansätze* for fully bound buffer variable V are shown in Table 3.4.

Methods	***U ansatz***	***Ansatz* parameters**
PadéA, PadéB, PadéExp	$U = \dfrac{2q}{A+r}$	$A = q\varepsilon + \sqrt{q^2\varepsilon^2 + 2q\lambda_1}$
ExpPadéA, ExpPadéB, ExpExp	$U = 2q\dfrac{1-e^{-ar}}{r}$	$a = \left(\sqrt{\varepsilon^2 + \lambda_1/q} - \varepsilon\right)\Big/\lambda_1$

Table 3.4 *Ansätze* for the Fully Bound Buffer Variable V and Equations for Their Parameters as Functions of Non-dimensional Model Parameters q, ε, λ_1, and λ_2. Parameters a and A from the corresponding *ansatz* for the free buffer variable U are showed in Table 3.3. For PadéB, ExpPadéB, PadéExp and ExpExp, parameter b_2 or s is given by the unique real positive root of a cubic equation obtained by combining equations in the last two columns, whose closed-form solutions are given in Appendix D.

Method	***V ansatz***	**Equations for *ansatz* parameters**
PadéA	$\dfrac{q^2}{r^2+b_1 r+b_2}$	$b_1 = 2q\left[1-q+\varepsilon\left(2q-1\right)\right]$ $b_2 = \dfrac{Aq+\sqrt{A^2q^2+16b_1Aq\lambda}}{4}$
PadéB		$b_1 = \dfrac{b_2}{2\lambda}\left(\dfrac{2b_2}{Aq}-1\right)$ $\lambda_2\left(\dfrac{b_1^2}{b_2}-1\right)+b_2^2\dfrac{q-2}{3qA^2}+\dfrac{b_1-2b_2}{6}=\dfrac{q\left(q-1\right)}{12}$
ExpPadéA		$b_1 = 2q\left[1-q+\varepsilon\left(2q-1\right)\right]$ $b_2 = \dfrac{q+\sqrt{q^2+16ab_1\lambda_2 q}}{4a}$
ExpPadéB		$b_1 = \dfrac{b_2}{2\lambda_2}\left(\dfrac{2ab_2}{q}-1\right)$ $\lambda_2\left(\dfrac{b_1^2}{b_2}-1\right)+b_2^2a^2\dfrac{2q-3}{6q}+\dfrac{b_1-2b_2}{6}=\dfrac{q\left(q-1\right)}{12}$
PadéExp	$q^2\dfrac{1-\exp\left(-sr\right)\left(1+sr\right)}{r^2}$	$4\lambda_2 s^3+3s^2-12/\left(qA\right)=0$
ExpExp		$4\lambda_2 s^3+3s^2-12a/q=0$

We will now illustrate this series interpolation method more concretely using the ExpPadéA approximant as an example. This *ansatz* is formed by combing Equation 3.24 for U and Equation 3.25 for V. Then, as indicated in Table 3.2, we constrain the values of *ansatz* parameters using terms of orders O(1) and O(r) in Equation 3.20 for both U and V,

and term of order $O(x^3)$ in Equation 3.22 for V (recall once again that all *ansätze* automatically match the term of order $O(x)$ in U and the term of order $O(x^2)$ in V). Therefore, we obtain 5 constraints for 5 unknowns (three parameters in ExpPadéA *ansatz*, plus U_0 and V_0):

$$\begin{cases} U_0 = 2qa,\ V_0 = q^2/b_2, \\ \left(\varepsilon U_0 - 1\right)/\lambda_1 = -qa^2, \\ \left(V_0 - U_0\right)/\left(2\lambda_2\right) = -q^2 b_1/b_2^2, \\ -b_1 q^2 = -2q^3\left[1 - q + \varepsilon\left(2q - 1\right)\right]. \end{cases} \tag{3.27}$$

The solution of this system is given in Tables 3.3-3.4. Note that the 3rd equation in this system leads to a quadratic equation for b_2, whose solution is given in Table 3.4.

3.2.2 Accuracy in Approximating Buffer and Ca^{2+} Concentrations

As a crude demonstration of the performance of our *ansätze*, Figure 3.1 shows our approximants for 4 select combinations of model parameters, with each column presenting the results for all concentration variables (b, b^*, b^{**}, c) for a particular set of values of λ_2, ν_2, γ, and ε, as labeled in the figure title. The accurate numerical results are shown as thick grey curves. Since the expressions for the free buffer b (specified by U) are identical for PadéA, PadéB, and PadéExp approximants (see Table 3.3), the corresponding approximation is labeled as U-Padé, and shown as a single *dashed green* curve in the top panels of Figure 3.1. Similarly, b approximants for ExpPadeA, ExpPadeB and ExpExp are also identical, and are labeled U-Exp and shown as a *dashed magenta* curves in the top panels. When showing results for variables b^*, b^{**}, and c in rows 2-4 of Figure 3.1, only

the best 5 approximants are shown for each parameter combination, which is a subset of the total of 7 approximants combining the 6 *ansätze* in Table 3.2, plus the RBA.

As will be elucidated further below (see Figures 3.3-3.6), the parameter regimes we selected in Figure 3.1 are not optimal for the *ansätze* we introduce; this is especially true for the parameter combinations in the last two columns of Figure 3.1. Nevertheless, even for the chosen sub-optimal parameter combinations, a decent qualitative agreement with the accurate numerical solution is achieved by at least one of the *ansätze*, with higher accuracy for the first two parameter combinations in Figures 3.1A1-4, B1-4. We observe that RBA can compete with the newly presented approximants only when diffusivity λ_2 is very small (Figure 3.1C1-C4); therefore, RBA is not shown for the other three parameter choices. Note the difference in scales in the different panels of Figure 3.1: some of the apparent large discrepancies for b^* and b^{**} involve relatively small absolute differences. The accuracy of several of the newly presented approximants is sufficiently high for the curves to completely overlap with the numerical simulations. Therefore, the series interpolation method achieves significant improvement of approximation accuracy for a wide range of model parameters, as compared to RBA.

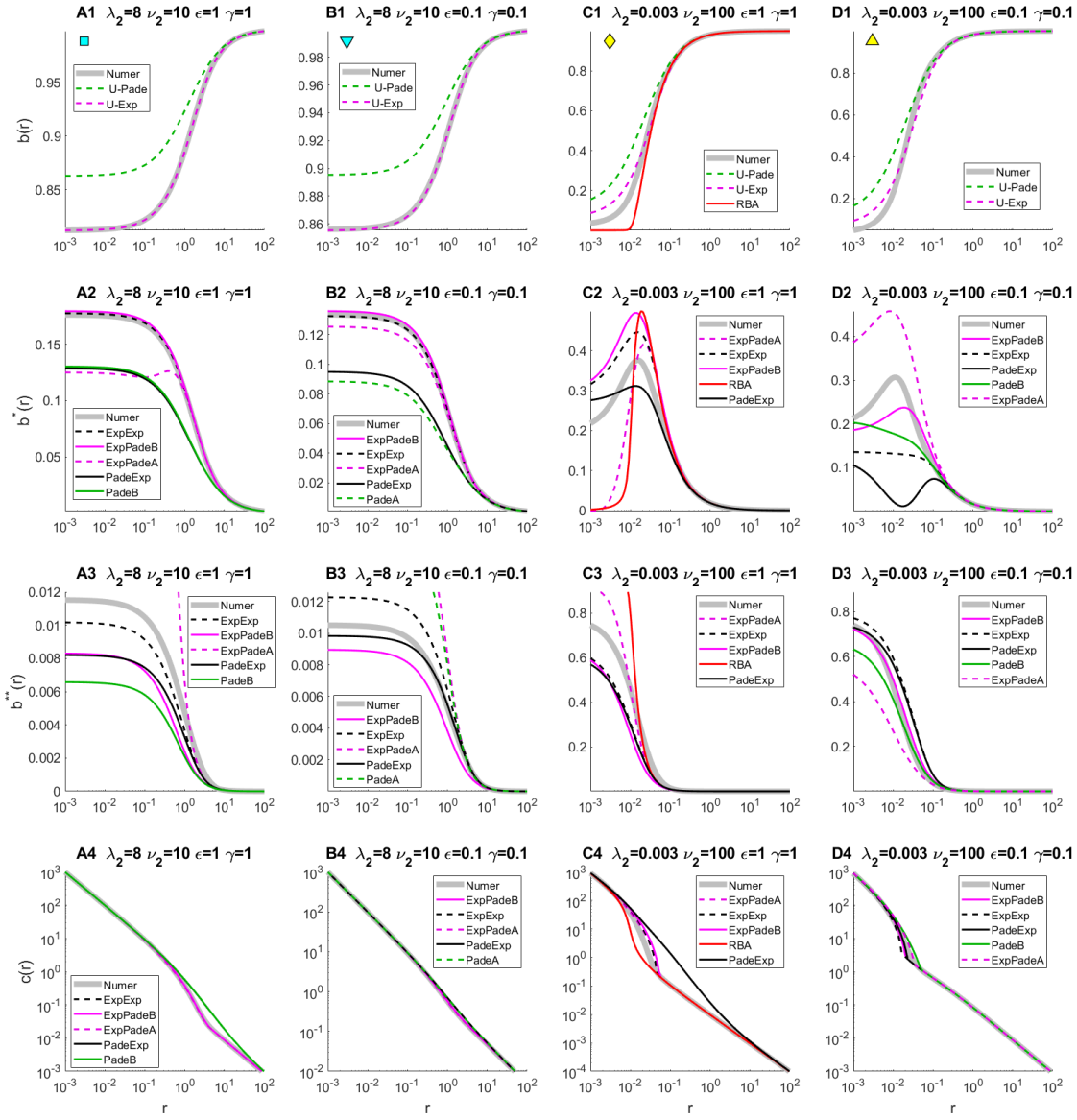

Figure 3.1 Comparison of approximations of equilibrium Ca^{2+}, free buffer, partially bound buffer, and fully bound buffer concentration, obtained using the newly developed series interpolation methods: PadéA (*green curves*), PadéB (*dashed green*), ExpPadéA (*magenta*), ExpPadéB (*dashed magenta*), PadéExp (*black*), ExpExp (*dashed black*), and RBA (*red*). Since these approximants involve only two different *ansätze* for the free buffer variable U (see Tables 3.2, 3.3), the latter are labeled as U-Pade (*dashed green*) and U-Exp (*dashed magenta*) in panels A1, B1, C1, D1. All panels show the respective dimensionless concentrations as a function of distance from the Ca^{2+} channel, for 4 distinct choices of model parameters λ_2, ν_2, γ, and ε. as indicated in the panel title. *Grey curves* show the accurate numerical simulations. A subset of 5 best methods is shown for each parameter combinations. The accuracy of some approximants is sufficiently high for the curves to completely overlap with the numerical solution, hence the difference between the curves is very small and hard to resolve by eye.

It is interesting to note that the partially-bound buffer concentration b^* is not necessarily monotonic with respect to distance from the origin, unlike the free and fully-bound concentration variables. Despite the simple functional forms of our *ansätze*, they can in fact reproduce this interesting non-monotonic behavior accurately, at least for some combination of model parameters: see for instance the ExpPadéB approximant in Figure 3.1D2.

Identifying the best approximations for fully bound buffer (b^{**}) and partially bound buffer (b^*) is a lot more difficult than choosing the best approximant for the free buffer (b) using data presented in Figure 3.1, since all approximants perform quite differently under varying conditions. ExpPadéA, ExpPadéB, and ExpExp give more consistently accurate results, but the pattern is difficult to summarize with only a couple parameter sets. As in the simple buffer case, buffer approximations have the lowest accuracy near the channel, and the greatest accuracy far from the channel, since buffer concentrations at the channel location are unknown, while the long-range asymptotic behavior of the true solution is known, and given by Equation 3.22. In contrast, the differences between distinct Ca^{2+} approximations and the numerical solution are shown on a logarithmic scale, and are more pronounced at intermediate distances from the channel, due to the dominance of the free source term $1/r$ near the channel (Equation 3.18), which is the same regardless of model parameter.

As we discussed before, Ca^{2+} concentrations shown in Figure 3.1 are obtained using Ca^{2+} conservation law (Equation 3.18), based on inexact approximations for b and b^{**}. Therefore, no direct physical constraints on Ca^{2+} are imposed by this procedure. For specific parameters regimes, this may result in negative values of $[Ca^{2+}]$ sufficiently far

from the channel, where the corresponding values of the true solution are positive but small. This usually happens for very large values of buffering strength, $\nu_{1,2} \geq 100$. When this occurs, we use the RBA approximation given by Equations F.10-F.12 in Appendix F as a lower bound on Ca^{2+}. This is justified since, as noted above, RBA becomes accurate sufficiently far from the channel, regardless of model parameters. Moreover, our extensive numerical investigation leads us to conjecture that RBA in fact represents a sub-solution for the true $[Ca^{2+}]$. This truncation by RBA from below helps us correct the errors in estimating Ca^{2+} for larger distances. Even in cases where negative $[Ca^{2+}]$ values detected at large distances are replaced with RBA values, the accuracy of the new methods at closer distances are significantly improved compared to the RBA solution, as is the case for instance in Figure 3.1C4.

Obviously, examining approximation behavior for several example parameters combinations is insufficient to unveil the complicated parameter-dependent accuracy of these approximations, and for some parameter sets the difference between several approximants in Figure 3.1 is impossible to tell by eye. Therefore, following prior work and what we did in Chapter 2 (19, 33, 34), we will more systematically explore the parameter-dependence of the absolute deviation between the given approximation and the accurate numerical solution, using the following norm, similar but slightly different from the norm used in the case of simple buffer (Equation 2.28):

$$\begin{aligned} \left\| b_{appr} - b_{num} \right\| &= \frac{1}{N\,p} \sum_{n=1}^{N} \left| b_{appr}(r_n) - b_{num}(r_n) \right|, \\ p &= \frac{1}{2} \left(\max_{r_n} \left| b_{appr}(r_n) \right| + \max_{r_n} \left| b_{num}(r_n) \right| \right), \\ r_n &= 10^{-3+5n/N}, n = 1, 2, \ldots N. \end{aligned} \tag{3.28}$$

Since we use the same error measure for approximating bound buffer states b^* and b^{**} as for b, we normalize by the maximal concentration in the denominator of Equation 3.28 to make it an even more stringent accuracy measure: as Figure 3.1 illustrates, the Ca^{2+}-bound buffer concentrations can be quite small in certain parameter regimes, as compared to free buffer b, which always approaches 1 as $r \to \infty$.

Since b^* (as well as c) is uniquely determined by b and b^{**} through the conservation law (Equation 3.17), in the figures below we focus on the sum of errors for b and b^{**}, instead of analyzing them individually. In Figure 3.2, we use this stringent error measure for a more systematic comparison of the accuracy of the new approximants. Namely, we plot the sum of errors in b and b^{**} for each approximant as a function of the buffering strength parameter ν_2 varying from 10^{-3} to 10^3, for three different fixed values of the buffer diffusivity parameter λ_2 (λ_2=0.1, λ_2=1, or λ_2=10) and two combinations of cooperativity parameters (ε, γ), similar to what we did in Chapter 2. To reveal the impact of Ca^{2+}-binding cooperativity on approximant performance, one choice of (ε, γ) values corresponds to a non-cooperative buffer (ε=γ=1, bottom panels in Figure 3.2), while the other choice corresponds to a very cooperative buffer (ε=γ=0.1, top panels in Figure 3.2). We no longer compare the approximants for b, b^* and b^{**} separately, since we are interested in selecting a single best approximation for each given parameter combination. The error of RBA (*red curves*) is also included for the sake of comparison.

For most combinations of parameters examined in Figure 3.2, ExpPadéA, ExpPadéB, and ExpExp achieve the best accuracy compared to other approximants, which is consistent with the results from Figure 3.1. For the non-cooperative case ε=γ=1 (bottom row of panels in Figure 3.2), the best approximating method is always ExpExp for

sufficiently large values of ν_2 and λ_2, and the error is always below 10%, which is very good for such a simple approximation and stringent error measure. For the cooperative buffer case, $\varepsilon=\gamma=0.1$ (top row in Figure 3.2), the individual error curves get more tangled, and the choice of best method is somewhat more complicated, but in general ExpExp achieves superior accuracy at smaller values of buffering strength ν_2. At larger values of ν_2, ExpPadéB becomes the best approximation method. As always, different methods need to be chosen to achieve the best accuracy of approximation for different parameter combinations.

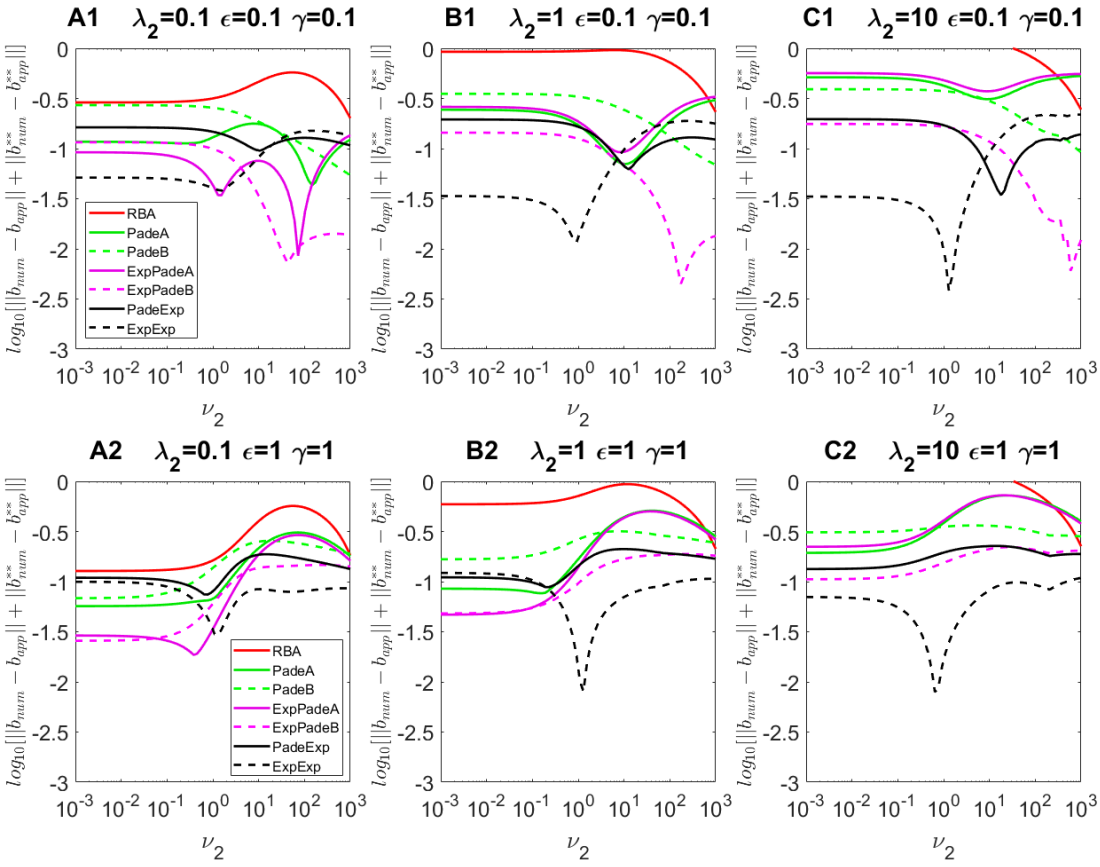

Figure 3.2 Accuracy comparison of the approximations for the combination of equilibrium nanodomain free buffer and fully bound buffer concentrations, obtained by the newly developed series interpolation methods: PadéA (*green curves*), PadéB (*dashed green curves*), ExpPadéA (*magenta curves*), Exp-PadéB (*dashed magenta curves*), PadéExp (*black curves*), and ExpExp (*dashed black curves*). RBA is also plotted for comparison purposes (red curves). All panels show the average error of the respective dimensionless concentrations (Equation 3.28) on base-10 logarithmic scale, as a function of model parameter ν_2 ranging from 10^{-3} to 10^{3}, for three distinct choices of fixed model parameter λ_2: λ_2=0.1, λ_2=1, and λ_2=10, with $\varepsilon = \gamma = 0.1$ (top row), and $\varepsilon = \gamma = 1$ (bottom row).

For the parameter conditions examined in Figure 3.2, RBA performs significantly worse than all of the newly developed methods. However, the advantage of RBA will be revealed for smaller values of $\lambda_{1,2}$, as will be clear in the results presented next.

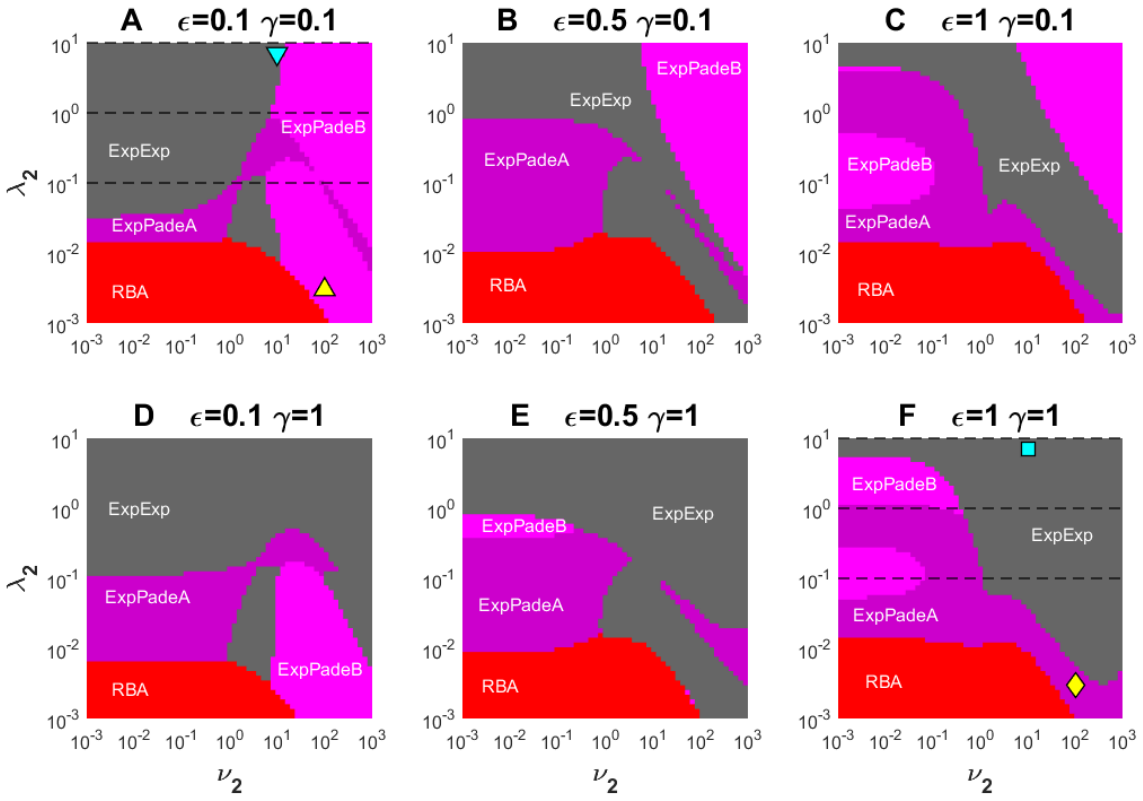

Figure 3.3 Comparison of parameter regions where a given approximant outperforms the rest in estimating the combined errors of free and fully bound buffer concentrations in the (ν_2, λ_2) parameter plane, according to the error measures given by Equation 3.28, with ε and γ fixed for 6 different choices: (A) ε=γ=0.1; (B) ε=0.5, γ=0.1; (C) ε=1, γ=0.1; (D) ε=0.1, γ=1; (E) ε=0.5, γ=1; (F) ε=γ=1. Each color in A through F marks the parameter region of best performance for the following approximants: RBA (*red*), ExpPadéA (*dark magenta*), ExpPadéB (*light magenta*), and ExpExp (*gray*). Yellow and cyan symbols mark parameter point corresponding to simulations in Figure 3.1, where the free and fully bound buffer concentrations are plotted separately. Dashed lines mark the locations of parameter scans in Figure 3.2.

Figure 3.3 summarizes and extends the results presented in Figure 3.2, labeling the best approximants for a wide range of buffer mobility λ_2 varying over 4 orders of magnitude, and ν_2 varying over 6 orders of magnitude, for 6 fixed sets of ε and γ values corresponding to each of the 6 panels. The selection of best approximant in Figure 3.3 is based on the minimal sum of errors of b and b^{**} estimates; the corresponding smallest error value is shown in Figure 3.4. As noted above, using this combined error measure helps in

determining the single best approximation method for a given set of model parameters, recalling that b^* and c are uniquely determined by b and b^{**} (Equation 3.17). Note that we exclude PádeExp, PádeA and PádeB methods in this comprehensive comparison: even though there are parameter regions where these three methods outperform others, these parameter regions are relatively small, and the accuracy advantage is not very significant. Figure 3.3 shows that there is still a significant portion of parameter space where RBA outperforms our newly developed methods, but only when $\lambda_{1,2}$ is sufficiently small. As Figure 3.4 shows good qualitative agreement, with accuracy within 10% is always guaranteed for all examined parameter combinations, and for some narrow parameter regimes the accuracy can be extremely high, with error reaching 0.025%.

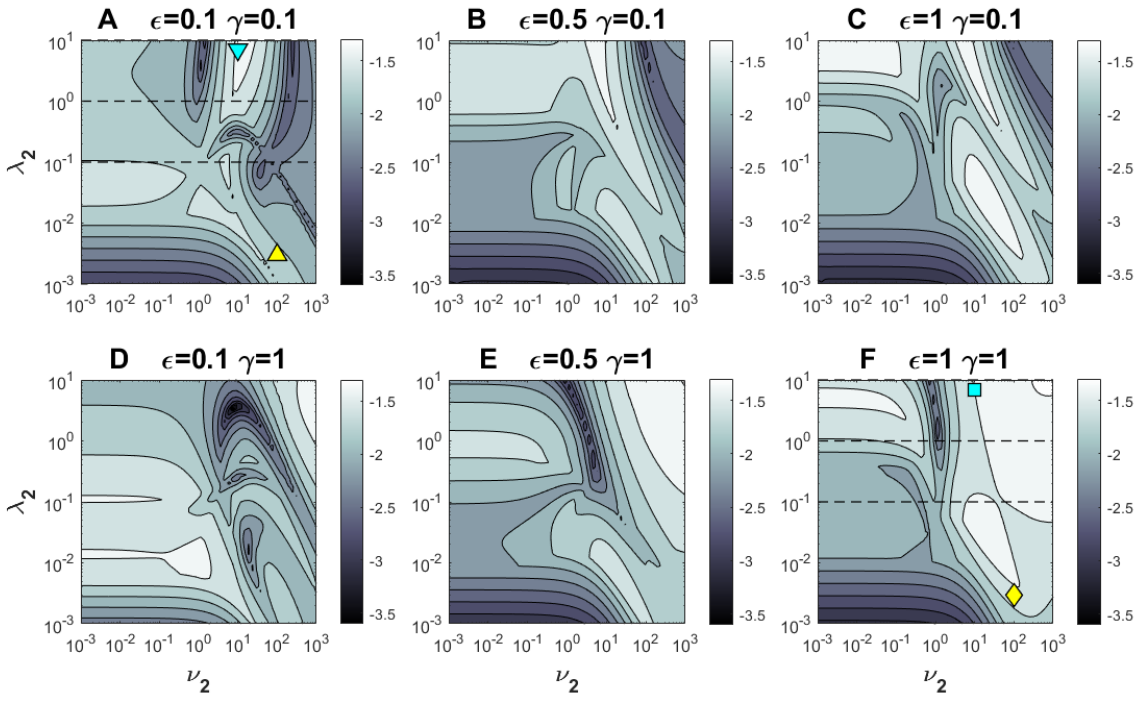

Figure 3.4 The smallest error in estimating the free and fully bound buffer concentrations in the (ν_2, λ_2) parameter plane, according to the error measures given by Equation 3.28, with ε and γ fixed to 6 different choices, as in Figure 3.3. The color scales in A through F indicate the log-10 error values. Darker shades represent better accuracy, according to the error bars on the right of each panel.

Even though Ca^{2+} is uniquely determined from the buffer concentrations by the Ca^{2+} conservation law, it is still useful to look at the performance of different approximants in estimating $[Ca^{2+}]$ in particular, since the latter is of clear physical importance and has a different behavior as a function of distance from the channel. As in the simple buffer case, close to the channel location $[Ca^{2+}]$ is dominated by the unbounded point source term, $1/r$, therefore we will use the same logarithm difference norm that we used in the case of simple buffer, given by Equation 2.36. We note that qualitatively this norm has the same behavior as the relative difference norm used by (19).

Figures 3.5 and 3.6 summarize the results on the most accurate method and the corresponding error in estimating $[Ca^{2+}]$, calculated using Equation 2.36, using the same parameter combinations as in Figures 3.3 and 3.4. From Figure 3.5, we can see that for any particular set of model parameters, the optimal approximants for $[Ca^{2+}]$ can be different from the optimal buffer approximant shown in Figure 3.3, despite the fact that $[Ca^{2+}]$ is directly calculated from buffer concentrations. As in the simple buffer case, the error in Ca^{2+} estimation measures the accuracy of our approximants at intermediate distance from the channel, while the error in buffer estimation reveals the method accuracy proximal to the channel location. This fact can also be observed in Figure 3.1.

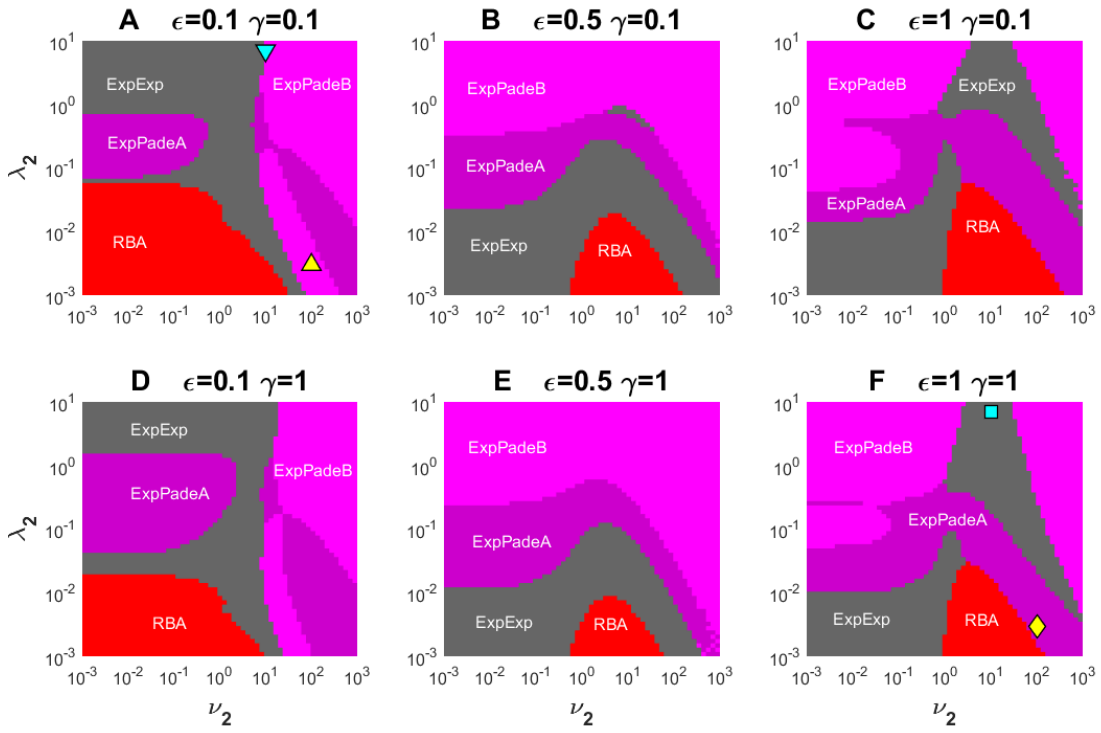

Figure 3.5 Comparison of parameter regions where a given approximant outperforms the rest in estimating $[Ca^{2+}]$ in the (ν_2, λ_2) parameter plane, according to the error measures given by Equation 2.36, with ε and γ fixed to 6 different choices, labeled in each panel. Each color in A through F marks the parameter region of best performance for the following approximants: RBA (*red*), ExpPadéA (*dark magenta*), ExpPadéB (*light magenta*), PadéExp (*black*), and ExpExp (*gray*). Yellow and cyan symbols mark parameter points corresponding to simulations in Figure 3.1.

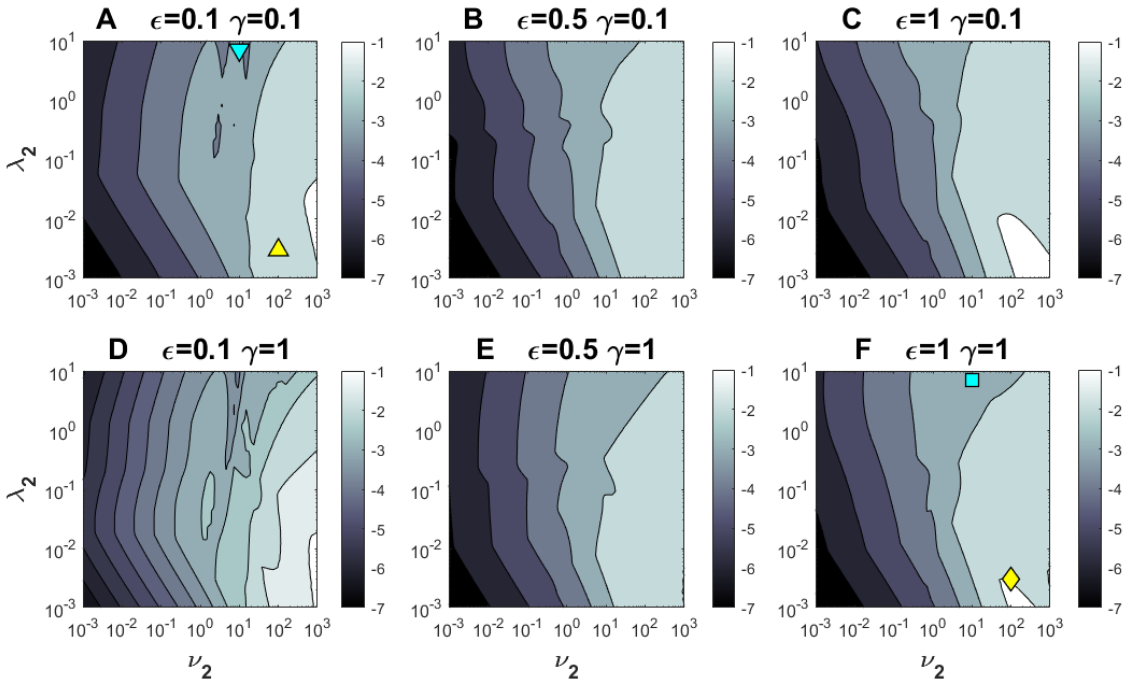

Figure 3.6 The smallest error in estimating [Ca^{2+}] in the (ν_2, λ_2) parameter plane, according to the error measure given by Equation 2.36, obtained using the best approximant shown in Figure 3.5 for each parameter point, with ε and γ fixed to 6 different choices, as in Figure 3.5. All parameter choices and layout are identical with Figures 3.3-3.5. The gray-scale in all panels indicates the log-10 error values, as indicated in scale bars to the right of each panel. Darker shade represents better accuracy.

Although PadéExp approximant is not taken into account in the comparisons contained in Figures 3.5 and 3.6, it outperforms other methods in limited regions of parameter space corresponding to small λ_2 and either very large or very small ν_2; however, even in those parameter regions, the advantage of PadéExp is not very significant.

In order to evaluate whether our newly developed approximants are indeed performing well in a wide range of parameters, in Figure 3.7 we simulate the Ca^{2+} nanodomain in the presence of 100μM of Ca^{2+} buffer with the properties of either calretinin or one of the two lobes of calmodulin, which all have extreme values of cooperativity parameters, as listed in Table 3.1 (37, 41). As first shown in (33), RBA achieves reasonable accuracy only for the N-lobe of calmodulin, which correspond to values $\lambda_2 = 1.8 \cdot 10^{-4}$ and

ν_2 =25.4, which is within the parameter regions where RBA works the best. However, our newly developed method, ExpPadéA and ExpPadéB, work remarkably well for C-lobe of calmodulin: the curves for b, b^*, b^{**}, and c corresponding to the approximations and the numerical simulations completely overlap at the chosen ordinate scale. For calretinin, ExpPadéB works the best, and demonstrates very reasonable accuracy. Although ExpPadéB fails to accurately describe the behavior of the single-bound calretinin concentration, the latter is very small in magnitude.

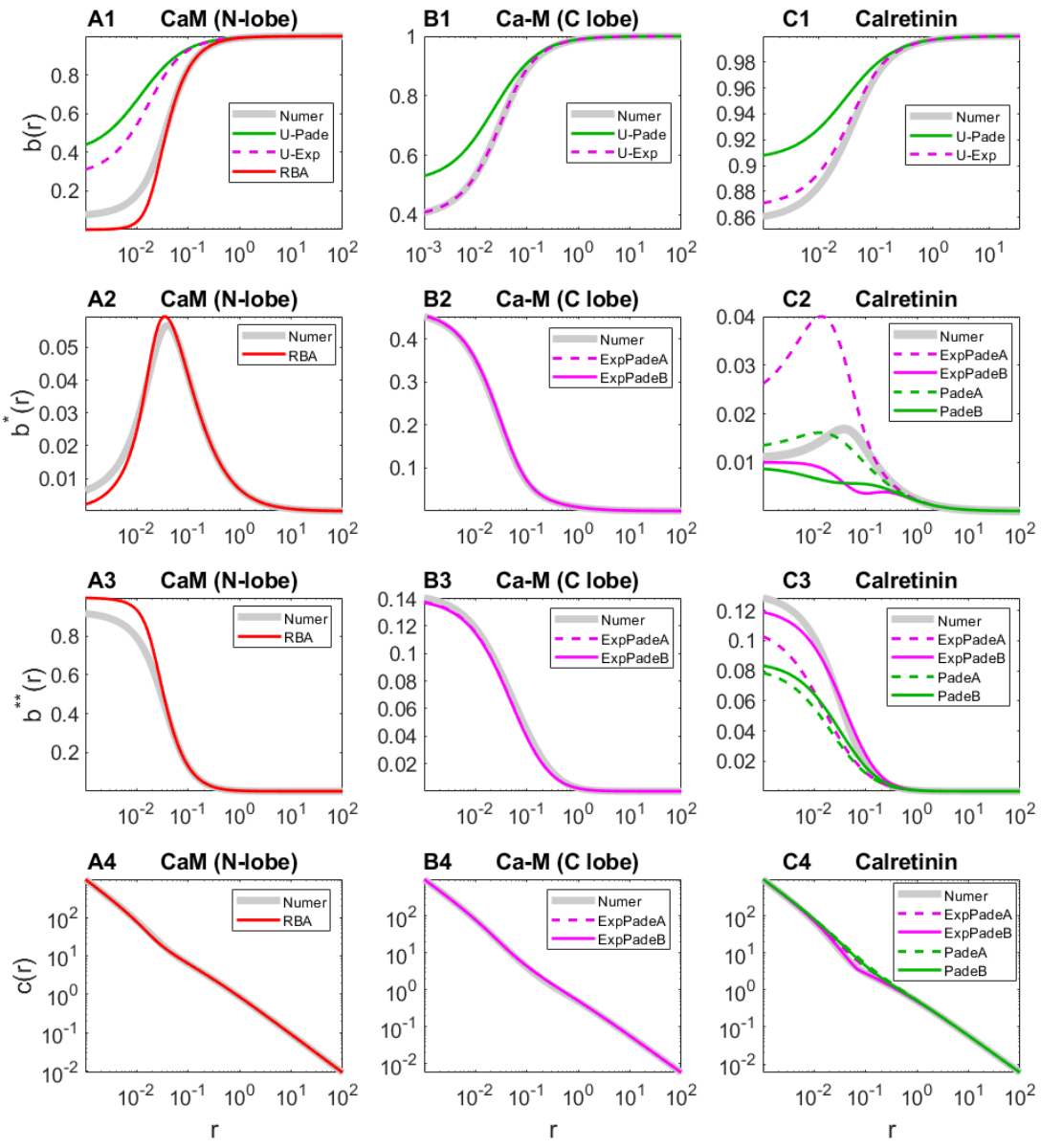

Figure 3.7 Approximation performance for the case of biological buffers, calmodulin N-lobe (A1-A4), calmodulin C-lobe (B1-B4), and calretinin (C1-C4), with parameters as in Table 3.1, corresponding to the current of I_{Ca}=0.4 pA, and total buffer concentration of 100 μM. As in Figure 3.1, approximants of free buffer concentrations in panels (A1, B1, C1) are labeled as U-Exp and U-Padé (see Tables 3.2-3.3), while only the best approximations are shown for the other concentration variables: ExpPadéA (*solid magenta curve*), ExpPadéB (*dashed magenta curve*), PadéA (*dashed green curve*), PadéB (*solid green curve*), and RBA (*red curve*). Accurate numerical results are shown as thick gray curves.

CHAPTER 4

DISCUSSION

4.1 Summary of Results and Discussion for Simple Buffer Case

We have presented a significant extension of prior modeling work on equilibrium single-channel Ca^{2+} nanodomains, based on two distinct approaches applied to several types of parametric approximants, which to our knowledge have not been considered previously. In particular, we extended the series interpolation methods recently used to construct rational function (Padé) approximants (34), generalizing it to more accurate and natural parametric forms given by Equations 2.25-2.27, which bear resemblance to the EBA and LIN approximants obtained previously using different methods. Furthermore, following a very useful suggestion by Dr. Muratov, we applied the variational approach to approximants of the same functional form, resulting in significant improvement of approximation accuracy for a wide range of parameters. As summarized in Figures 2.6-2.7, a combination of previously developed and newly presented approximants can achieve an excellent estimation for the free buffer and Ca^{2+} concentration near an open channel, for several orders of magnitude of dimensionless parameters λ, ν, and η. Further, we showed that a subset of just three approximation methods, Padé2, RBA2 and DblExp-Global, allow to achieve an average accuracy of 1% or better in the entire parameter range that we explored. As Figures 2.6 and 2.7 show, the parameter region posing the greatest challenge corresponds to $\lambda << 1$, $\nu >> 1$. However, Figures 2.1B, 2.2A, 2.3B, 2.4A and 2.5A demonstrate that reasonable accuracy is achieved even in this parameter regime.

We note that the accuracy profiles shown in the Figures 2.2, 2.4-2.7 depend on our choice of the error measures, given by Equations 2.28, 2.36. For instance, without spacing mesh points logarithmically in these error measures, the accuracy ranking of different methods may change. However, this error measure choice provides a very demanding and restrictive comparison, covering a very wide range of distances, and weighting the error more at short distance from the channel (19, 33, 34). Therefore, we believe that the chosen error measures are appropriate and yield the best comparison method given the wide range of parameters we consider. Further, we checked that the conclusions are not substantially changed if the L^{∞} norm is chosen instead.

The drawback of the methods we present is that the expression for approximant parameters can be quite complex, especially for the *ansätze* with more than one exponential term. The level of complexity of different methods is not the same: the simplest ones are the mono-exponential approximants (Exp-Ser, Exp-Var, Exp-Global), followed by double-exponential methods that require finding a root of a cubic equation (DblExp-Ser, DblExp-Var, DblExp-Global), and finally, two methods, Exp-Padé and Padé2, require solving a fourth-order polynomial system. However, all approximants were determined as closed-form expressions that only take several lines of computer code (see Appendix A, B).

Several other functional forms not shown in Table 2.2 were also considered but are not presented here since they either did not result in better accuracy compared to other approximants or provide only a minor improvement in limited regions of parameter space while complicating the expressions for parameters. This is true for example for the double-exponential approximation given by Equation 2.25 but with two different exponent parameters, α_1 and α_2. However, it is possible that we missed other accurate approximants.

It is possible that such improved *ansätze* could be found, for instance by taking into account the singularities of the analytic extension of the buffer concentration to the unphysical complex-distance plane. We note that only RBA captures the branch cut of this analytic extension, which jumps from the physical value b=1 at $x=0^+$ ($r=+\infty$) to the unphysical value $b = -\eta / \nu$ at $x=0^-$ ($r=-\infty$) (see Figure 7 in (34)). Further, as noted above, 2nd-order RBA derived in (19) agrees with the long-range asymptotic expansion of the true solution given by Equation 2.22 up to terms of order x^5 (19, 34). Therefore, our initial efforts to construct an improved *ansatz* were based on modifying the RBA approximant. However, so far, we failed to find a successful modification of RBA that improves its performance.

4.2 Summary of Results and Discussion for Complex Buffer Case

We have successfully extended some of the approaches we introduced for the case of simple buffer to the study of nanodomains in the presence of complex buffers with more realistic Ca^{2+} binding properties. In previous studies, only RBA has been extended to complex buffers, and only to 1st order (33). In Chapter 3, we demonstrated that the series interpolation approach presented in Chapter 2 can be applied to such buffers, once again using a combination of simple rational and exponential functions. As summarized in Figures 3.3-3.6, the newly presented approximants achieve good qualitative accuracy in estimating the buffer and Ca^{2+} concentration for complex buffer case, in a wide range of parameter regions. RBA is still superior for the cases with extreme parameter conditions, normally when non-dimensional diffusivities $\lambda_{1,2}$ are very small. Compared with RBA, the new approximation methods show more uniform error dependence for several orders of magnitude of dimensionless parameters λ_2, ν_2, γ, and ε. As Figures 3.4 and 3.6 show, with the contribution of new approximants, the combined error for the free and fully bound

buffer concentrations is within 10% in the wider parameter range that we considered, and the error in estimating Ca^{2+} is roughly of the same magnitude, albeit requiring artificially imposing the physical constraints $Ca^{2+}>0$ for very large values of buffering strength $\nu_{1,2}$. Additionally, from Figures 3.3 and 3.5, we can see that we can achieve this level of qualitative accuracy in the entire parameter range we consider with only three out of the total of 6 approximants, namely ExpPadéA, ExpPadéB, ExpExp, in addition to RBA. Figure 3.7 further shows that qualitative agreement can be achieved even with more extreme model parameter values corresponding to calretinin or one of the two lobes of calmodulin, which correspond to parameter combinations shown in Table 3.1.

Of course, practical use of the proposed approximant requires an algorithm for the choice of a particular *ansatz*, given a particular set of model parameters, without knowing the exact solution. Figures 3.3 and 3.5 provide a first step towards developing such an algorithm. Although the boundaries between parameter regions of best performance look complicated, a smaller subset of only three methods can allow one to develop a simple approximant selection algorithm, without sacrificing too much accuracy. Further, note that all of the best approximants (ExpPadeA, ExpPadeB and ExpExp) involve the same exponential *ansatz* for the free buffer variable, and the boundary of the corresponding region of best performance, relative to RBA, is as simple to specify as it is for the simple buffer case (compare Figure 2.6 and Figure 3.3). Here we note that, just like in the case of simple buffer analyzed in Chapter 2, the decision on the best algorithm, summarized in Figures 3.3-3.6, depends on the particular norm that we have chosen for comparison to the true solution, given by Equations 2.36 and 3.28.

Similar to series interpolation method for simple buffer, one of the drawbacks for the new methods we presented here is the complicated algebra expressions for the approximant parameters. For PadéB, ExpPadéB, PadéExp, and ExpExp, some of their *ansatz* parameters require finding the root of cubic equations. For PadéA and ExpPadéA, the level of complexity is lower, which only require solving the quadratic systems. However, all close-form expressions for the new approximants can be found efficiently using very brief computer code (see Appendix D), so the advantage of using these approximations compared to solving the original systems numerically is obvious.

Given how simple all of our approximants are, it is unlikely that we have exhausted all possible relatively accurate approximants, therefore improved *ansätze* could still be found. This is particularly true for the case of non-zero background Ca^{2+} concentration examined in Appendix E, which is a more challenging case and was not examined in as much detail as the case $c_\infty=0$. Therefore, there is more potential for improvement in this regard. Several functional forms other than what we have shown in Equations 3.23-3.26 were considered, but are not presented here due to either insufficient performance or lack of closed-form solutions for parameters.

Further, a lot of fundamental mathematical analysis for the complex buffer case, along the lines of analysis in Appendix 4 of (48), is yet to be performed. For instance, we did not provide a rigorous existence and uniqueness analysis for the weak equilibrium solution in the complex buffer case, nor a rigorous proof that RBA is a sub-solution for $[Ca^{2+}]$ in this problem. Finally, the feasibility of extending the variational method used in Chapter 2 to buffers with two binding sites is still an open question. One should explore in

particular the applicability of the multifunction variational method described in (49), and the Nash Point Equilibrium method, described in (50).

4.3 Future Extensions of Work on Equilibrium Ca^{2+} Nanodomain Approximation

There are many directions for extending and improving this work, apart from the open questions already noted above. One of the most significant challenges is relaxing some of the key simplifying assumptions of our nanodomain model, namely (1) allowing for simple volumetric Ca^{2+} extrusion (sink) to model homeostatic Ca^{2+} regulation, (2) extension to a Ca^{2+} channel pore of a finite width, and (3) exploring the generalization of these methods to the case of two or more channels. As far as the latter point is concerned, we note that LIN and RBA do allow an arbitrary number of channels and buffers (albeit at the expense of greater complexity), which is a significant strength of these two previously developed methods, despite their accuracy limitations. Further, Falcke et al (16) derived a closed-form equilibrium nanodomain result in the case of a homogeneous Ca^{2+} sink and finite channel pore radius; however, that work did not consider the important non-linear buffering terms. Since a homogeneous Ca^{2+} sink is equivalent to a non-saturable buffer, the latter study can be considered as a generalization of the EBA approximation.

Finally, as noted above, the utility of our approximants for both the simple and complex buffer case would be improved if one could find a method of estimating the method accuracy with respect to the chosen norms, without knowing the accurate numerical solution. For instance, one could examine whether barrier functions (sub- and super-solutions) could be used to establish the bounds on the approximant accuracy (47).

Our results for both simple and complex buffers demonstrate that the accuracy profile of the approximants we introduce is highly non-trivial, with the errors surface

having large dips for certain parameter combinations. This is potentially of interest and may reveal interesting properties of the underlying true solutions, deserving a careful investigation in the future.

More importantly, the newly developed approximants can be used to study in detail the parameter dependence of equilibrium concentrations of Ca^{2+} and buffer, which we showed to be especially non-trivial for a buffer with two binding sites. For example, the results shown in Figure 3.1 already reveal an interesting non-monotonic dependence of single-bound buffer on the distance from the Ca^{2+} channel for some, but not all, model parameters. Since most buffers have dual Ca^{2+} buffering and sensing roles, with partially and fully bound buffer having distinct affinities to downstream biochemical targets (35, 36), such non-trivial aspects of the equilibrium solutions may have physiological significance, to be investigated in detail.

Finally, for both the simple and the complex buffer case, our work is based on the assumption that the stationary solution of the reaction-diffusion equations can achieve sufficient accuracy in estimating Ca^{2+} concentration in the vicinity of a Ca^{2+} channel. We assume that the stationary Ca^{2+} nanodomains are established almost instantly and ignore the transient dynamics before the equilibrium is reached. However, the characteristic time needed to reach the steady state should be properly examined for a wide range of parameter values. Some related work on the time scale of the transients in reaction-diffusion systems can be found in (51).

APPENDIX A

EXPONENT PARAMETER FOR DOUBLE EXPONENTIAL APPROXIMATIONS FOR SIMPLE BUFFER

For each of the three approximation methods summarized in Table 2.2, the parameter α of the double-exponential *ansatz* satisfies a cubic equation of form:

$$\eta q^2 P\alpha^3 - Q\alpha^2 - R\alpha + 1/q = 0\,. \tag{A.1}$$

The three roots of this cubic can be succintly represented in the folowing form:

$$\alpha_k = \frac{1}{W}\left[Q - G_k - \frac{E}{G_k}\right] \; where \begin{cases} W = 3\eta q^2 P, \quad E = Q^2 + WR, \\ F = \frac{3}{2}\left(QR - SW\right)W + Q^3, \\ G_k = p_k\left[\sqrt{F^2 - E^3} + F\right]^{1/3}. \end{cases} \tag{A.2}$$

The constants p_k $(k = 1,2,3)$ in the expression for the intermediate quantity G_k denote branches of $(-1)^{1/3}$:

$$p_1 = \left(1 + i\sqrt{3}\right)/2,\; p_2 = \left(1 - i\sqrt{3}\right)/2,\; p_3 = -1\,. \tag{A.3}$$

In this notation, the real positive root of Equation A.1 corresponds to the value α_1 when implemented verbatim in MATLAB (Mathworks, Inc). For each of the three double-exponential approximants, the imaginary part of the root becomes non-zero for

small values of ν and λ corresponding to the inner region marked by thin curves in Figure 2.6A1, B1.

APPENDIX B

PARAMETERS OF THE EXP-PADÉ APPROXIMATION FOR SIMPLE BUFFER

For the Exp-Padé *ansatz* (Equation 2.27), matching the relationship between the first three terms in the Taylor series of the solution (Equation 2.20) leads to the following algebraic system for the *ansatz* parameters α and β:

$$\begin{cases} \beta = \eta q^3 \left[q\alpha\left(\lambda\alpha + 1\right) - 1 \right]^{-1}, \\ \dfrac{1-2\eta q}{2\eta q^2}\left(\alpha\beta\right)^2 + \left(\lambda\alpha + 2\eta q\right)\left(\alpha\beta\right) + 6\lambda - \eta^2 q^3 = 0. \end{cases} \tag{B.1}$$

This leads to a fourth-order polynomial equation for α, with the following explicit solution:

$$\alpha = \frac{1}{2\lambda}\left[H^{1/2} - Q + \left(2VH^{-1/2} - H - 6U \right)^{1/2} \right], \tag{B.2}$$

where constants U, V, H, Q are determined by model parameters $\{\lambda, q, \eta\}$ according to

$$
\begin{aligned}
&P = 6 + \frac{\eta q^2 \left(1 - \eta q\right)}{\lambda},\ Q = \frac{1}{P}\left(6 + \frac{\eta q^2}{2\lambda}\right),\\
&R = Q\left(1 - \frac{2\lambda}{q}\right) + \frac{2\eta^2 q^2}{P},\ U = \frac{R}{3} - \frac{Q^2}{2},\\
&V = Q\left(R - Q^2\right) + \frac{12\lambda}{qP},\\
&W = Q^2\left(\frac{R}{3} - \frac{Q^2}{4}\right) + 4\lambda\frac{6\left(Q + \lambda/q\right) - \eta^2 q^2}{3qP},\\
&E = V^2\left(\frac{V^2}{4} + U\left(U^2 - 3W\right)\right) - W\left(W - 3U^2\right)^2,\\
&G = \frac{V^2}{2} + U\left(U^2 - 3W\right) + E^{1/2},\\
&H = \frac{W + U^2}{G^{1/3}} + G^{1/3} - 2U.
\end{aligned}
\tag{B.3}
$$

We note that the other three roots do not yield real positive values of α and β. In the parameter regime $1\text{-}q\eta < 10^{-2}$ and $\lambda < 10^{-2}$, these expressions suffer from numerical loss of significance due to subtraction of values close in magnitude, in several of the intermeidate variables. The loss of accuracy can be corrected by an algebraic manipulation of the terms, by using higher-precision computation, or by applying a couple Newton's iteration steps to the computed root value.

APPENDIX C

PARAMETERS OF THE PADÉ2 APPROXIMATION FOR SIMPLE BUFFER

For the Padé2 rational function *ansatz* listed in Table 2.1, matching the long- and short-distance series solutions leads to a 4th order polynomial system (34), which has the following solution for the coefficients $A_{1,2}$ and $B_{1,2}$:

$$\begin{cases} B_2 = \dfrac{q}{R}\left(Q + G^{1/3} + \dfrac{H}{G^{1/3}} \right), \\ B_1 = \dfrac{1}{V}\left[\dfrac{B_2\left(B_2 R - 3qK\right)}{6\lambda q^2} - J \right], \\ A_1 = B_1 - q, \\ A_2 = B_2 - q(B_1 - \eta q^2), \end{cases} \tag{C.1}$$

where constants Q, G, H, R, K, J and V are determined by model parameters $\{\lambda, q, \eta\}$ and $p=q\nu$ according to

$$
\begin{aligned}
R &= 24\lambda - 3pq(p-2), \\
K &= 8\lambda^2 - 2\lambda q(2p^2 - 5p - 2) - pq^2(p-2), \\
Q &= K + 24\lambda^2 - 4\lambda pq(2p-3), \\
V &= 2\lambda(p+6) + pq(p-3)(p-2), \\
F &= 6\lambda^2 - \lambda q(p+3)(p-2) - \eta p q^3(2p-3), \\
J &= 24\lambda^2 - 2\lambda pq(5p-8) - \eta p^2 q^3(p-2), \\
E &= 12\lambda^2 + \eta\, p q^2\left(8\lambda + \eta p q^2\right), \\
H &= 1600\lambda^4 - 104\lambda^3 q(p-2)(9p+4) \\
&\quad + 4\lambda^2 q^2(39p^4 - 87p^3 - 63p^2 + 184p + 4) \\
&\quad - 4\lambda pq^3(p-2)(6p^3 - 21p^2 + 20p + 2) + p^2 q^4(p-2)^2, \\
W &= 12000\lambda^5 - 4\lambda^4 q(2687p^2 - 2966p - 553) \\
&\quad + 4\lambda^3 q^2(729p^4 - 1626p^3 + 486p^2 + 421p + 70) \\
&\quad - \lambda^2 q^3(243p^6 - 810p^5 + 609p^4 + 210p^3 - 21p^2 - 240p - 4) \\
&\quad - 2\lambda\eta\, p q^5(p-2)(20p^2 - 13p - 1) + p^2\eta^2 q^7, \\
G &= Q^3 + 2\lambda R\left[3QF - 9\lambda ER + V(-3qW)^{1/2}\right].
\end{aligned}
\tag{C.2}
$$

APPENDIX D

PARAMETERS OF PADÉB, EXPPADÉB, PADÉEXP, AND EXPEXP APPROXIMATIONS FOR COMPLEX BUFFER

For PadéB and ExpPadéB approximation, matching the coefficients of the short- and long-range series expansions leads to cubic systems for the *ansatz* parameter b_2 shown in Table 3.4, with the following explicit solution:

$$b_2 = q\left(Y + G + \frac{F}{G} \right) . \tag{D.1}$$

For PadéB, the auxiliary quantities Y, G, F are determined by

$$\begin{aligned} G &= \left(\sqrt{E^2 - F^3} + E \right)^{1/3}, \\ E &= Y^3 - YW + \lambda_2 X, \\ F &= Y^2 - \frac{2}{3} W, \\ X &= A^2 \frac{q - 1 + 12\lambda_2 q^{-1}}{24}, \\ Y &= \frac{5A + 2\lambda_2 (2 - q)}{18}, \\ W &= A^2 \frac{1 - 2\lambda_2}{12}, \end{aligned} \tag{D.2}$$

where the value of *ansatz* parameter A is shown in Table 3.3.

For ExpPadéB, the computation of b_2 value is the same as above, except for the redefinition of the following auxiliary quantities:

$$
\begin{aligned}
X &= \frac{q-1+12\lambda_2 q^{-1}}{24a^2}, \\
Y &= \frac{5+\lambda_2\, a\left(3-2q\right)}{18a}, \\
W &= \frac{1-2\lambda_2}{12a^2},
\end{aligned}
\tag{D.3}
$$

where parameter a is the ExpPadéB *ansatz* parameter shown in Table 3.3.

For both PadéExp and ExpExp approximations, the explicit solution of *ansatz* parameter s has the same form:

$$
s = G + \frac{Y^2}{G} - Y\,. \tag{D.4}
$$

For the PadéExp method, the auxiliary quantities G and Y are determined by

$$
\begin{aligned}
G &= \left(\sqrt{E^2 - Y^6} - E\right)^{1/3}, \\
E &= Y\left(Y^2 - \frac{6}{Aq}\right), \\
Y &= \frac{1}{4\lambda_2},
\end{aligned}
\tag{D.5}
$$

where the value of constant A is given in Table 3.3.

For the ExpExp method, all expressions are the same, except that quantity E is now given by

$$E = Y\left(Y^2 - \frac{6a}{q} \right), \tag{D.6}$$

where the value of constant a is given in Table 3.3.

APPENDIX E

THE CASE OF NON-ZERO BACKGROUND CA^{2+} CONCENTRATION FOR COMPLEX BUFFER

In the case of non-zero [Ca^{2+}] infinitely far from channel, the equilibrium relationships given by Equation 3.9, are transformed to the form (recall that in our non-dimensionalization b_∞=1):

$$\begin{cases} b_\infty^{\ *} = 2\varepsilon c_\infty, \\ b_\infty^{\ **} = \dfrac{c_\infty b_\infty^{\ *}}{2} = \varepsilon c_\infty^2. \end{cases} \tag{E.1}$$

Therefore, the total concentration parameters given by Equation 3.14 are uniquely determined by the non-dimensional background Ca^{2+} concentration, c_∞:

$$\begin{cases} b_T = 1 + b_\infty^* + b_\infty^{**} = 1 + \varepsilon c_\infty \left(2 + c_\infty\right), \\ c_T = c_\infty + \dfrac{\nu_2}{2}\left(b_\infty^* + 2b_\infty^{**}\right) = c_\infty \left[1 + \nu_1 \left(1 + c_\infty\right)\right]. \end{cases} \tag{E.2}$$

Similar to our analysis for the case c_∞=0, we simplify Equation 3.13 using the transformation $U=(b_T-b)/\varepsilon$, $V=b^{**}/\varepsilon$. This transforms Equation 3.18 to the following form, analogous to Equation 3.19:

$$\begin{cases} \lambda_1 \nabla^2 U &= 2\left[\dfrac{1}{r} - \dfrac{\varepsilon\nu}{2}\left(U+V\right) + c_T\right]\left(\varepsilon U - b_T\right) + U - V, \\ \lambda_2 \nabla^2 V &= \left[\dfrac{1}{r} - \dfrac{\varepsilon\nu}{2}\left(U+V\right) + c_T\right]\left(V - U\right) + 2V. \end{cases} \tag{E.3}$$

Note that U nor V are now non-zero infinitely far from the Ca^{2+} channel, approaching the values

$$\begin{cases} U_\infty = \dfrac{b_T - 1}{\varepsilon} = c_\infty \left(2 + c_\infty\right), \\ V_\infty = \dfrac{b_\infty^{**}}{\varepsilon} = c_\infty^2. \end{cases} \tag{E.4}$$

Here we will consider the Taylor series of the solution only up to order O(r) (cf. Equation 3.20):

$$\begin{cases} U = U_0 + \dfrac{\varepsilon U_0 - b_T}{\lambda_1} r + O(r^2), \\ V = V_0 + \dfrac{V_0 - U_0}{2\lambda_2} r + O(r^2), \end{cases} \tag{E.5}$$

where U_0=U(0) and V_0=V(0) are related to the concentrations of free and fully bound buffer at channel location, r=0; both are unknown *a priori*, as in the case c_∞=0. Using the transformation x=1/r, we obtain the long-range asymptotic expansion of the solution in powers of x (cf. Equation 3.22):

$$\begin{cases} U = U_\infty + 2q\left(c_\infty + 1\right)x + b_T q^3 \left[4\left(1-\varepsilon\right) - b_T\left(3 + \nu_1\right)\right]x^2 + O\left(x^3\right), \\ V = V_\infty + 2qc_\infty\left(1 + \varepsilon c_\infty\right)x + b_T q^3 \left[1 + \nu_1 b_T - \varepsilon c_\infty^2\left(3 + 2\varepsilon c_\infty\right)\right]x^2 + O\left(x^3\right). \end{cases} \tag{E.6}$$

However, the generalization of parameter q has a more complex form than in the case c_∞=0:

$$q = \frac{1}{b_T\left(1+\nu_1\right)+2\nu_1 c_\infty\left(1-\varepsilon\right)}. \tag{E.7}$$

It is important to note that the long-range V series shown above starts with terms of order O(1) and O(x), in contrast to the case c_∞=0, in which case V series starts with terms of order O(x^2) (see Equation 3.22). The reason is intuitively clear: if $c_\infty \neq 0$, then a non-zero fraction of buffer will be fully bound even infinitely far from the channel. In contrast, in the case c_∞=0, both bound buffer states approach zero as $r \to +\infty$ and $c_\infty \to 0$, with fully bound buffer decaying faster than single-bound buffer and [Ca^{2+}], which explains the quadratic dominant term in $V(x)$ in that case.

Because of the U and V long-range asymptotic series behavior noted above, the simplest approximants involve exponential and the 1st order (bilinear) Páde approximants. Like in the case c_∞=0, we find that the best approximants achieving sufficient accuracy in large portions of parameter space are the analogues of the ExpExp and ExpPáde approximants considered above. Namely, we choose the exponential *ansatz* for the free buffer variable U, analogous to Equation 3.24:

$$U\left(r\right) = U_\infty + 2q\left(1+c_\infty\right)\frac{1-\exp\left(-\alpha_1 r\right)}{r}. \tag{E.8}$$

Note that it matches Equation E.6 to order O(x). In contrast, best V approximant accepts two possible simplest forms, which define the approximant type, and match Equation E.6 to the same order O(x):

- ExpExp: *ansatz* for V is also an exponential, with one free parameter α_2:

$$V(r) = V_\infty + 2qc_\infty(1+\varepsilon c_\infty)\frac{1-\exp(-\alpha_2 r)}{r}. \tag{E.9}$$

- PadéExp: *ansatz* for V is a bilinear function, with one free parameter β:

$$V(r) = V_\infty + \frac{2qc_\infty(1+\varepsilon c_\infty)}{\beta + r}. \tag{E.10}$$

We will now provide the derivation of the free parameters in above *ansätze*, in terms of model parameter values. We start with the free parameter α_1 in the U *ansatz*, Equation E.8, which we Taylor expand to obtain

$$U = U_\infty + 2\alpha_1 q(1+c_\infty) - q\alpha_1^2(1+c_\infty)r + O(r^2). \tag{E.11}$$

We then match this expansion to terms up to order O(r) in Equation E.5, which yields an equation

$$-q\alpha_1^2(1+c_\infty)\lambda_1 = \varepsilon\left[U_\infty + 2\alpha_1 q(1+c_\infty)\right] - b_T. \tag{E.12}$$

This is a quadratic equation for the unknown parameter α_1. Since $b_T - \varepsilon U_\infty = 1$ according to Equation E.4, we find that this equation always has one real positive root:

$$\alpha_1 = \frac{\varepsilon}{\lambda_1}\left[\sqrt{1 + \frac{\lambda_1}{q\varepsilon^2(1+c_\infty)}} - 1\right]. \tag{E.13}$$

Having constrained the *U ansatz*, we now constrain the free parameter in each of the two simple *V* approximants that we consider:

- ExpExp: expanding the *V ansatz* in Equation E.9, we obtain

$$V = V_\infty - 2\alpha_2 q c_\infty \left(1+\varepsilon c_\infty\right) - q\alpha_2^2 c_\infty \left(1+\varepsilon c_\infty\right) r + O(r^2). \tag{E.14}$$

Matching this expansion with terms up to order O(*r*) in Equation E.5, and using the expansion in Equation E.11 to obtain the approximation for U_0, we obtain a quadratic equation for α_2:

$$-2\lambda_2 q\alpha_2^2 c_\infty \left(1+\varepsilon c_\infty\right) = V_\infty - 2\alpha_2 q c_\infty \left(1+\varepsilon c_\infty\right) - U_\infty - 2\alpha_1 q\left(1+c_\infty\right). \tag{E.15}$$

Since $U_\infty - V_\infty = 2c_\infty$ according to Equation E.4, we obtain the real positive root

$$\alpha_2 = \frac{1}{2\lambda_2}\left[\sqrt{1+4\lambda_2 \frac{\alpha_1 q\left(1+c_\infty\right)+c_\infty}{c_\infty q\left(1+\varepsilon c_\infty\right)}} - 1\right]. \tag{E.16}$$

- PadéExp: expanding the *V ansatz* in Equation E.10, we obtain

$$V = V_\infty + \frac{2qc_\infty\left(1+\varepsilon c_\infty\right)}{\beta}\left(1-\frac{r}{\beta}\right). \tag{E.17}$$

Matching this expansion with terms up to order O(*r*) in Equation E.5, and multiplying by β^2, yields an equation

$$\beta^2 \lambda_2 + \beta + \frac{V_\infty - U_0}{2qc_\infty\left(1+\varepsilon c_\infty\right)} = 0, \tag{E.18}$$

where $U_0 = U_\infty + 2\alpha_1 q\left(1+c_\infty\right)$ according to Equation E.11. Since $U_\infty - V_\infty = 2c_\infty$ according to Equation E.4, we obtain a real positive root for all model parameter values:

$$\beta = \frac{1+\sqrt{1+8\lambda_2 F}}{2F}, \tag{E.19}$$

where

$$F = \frac{U_0 - V_\infty}{2qc_\infty\left(1+\varepsilon c_\infty\right)} = \frac{c_\infty + q\alpha_1\left(1+c_\infty\right)}{qc_\infty\left(1+\varepsilon c_\infty\right)}, \tag{E.20}$$

and α_1 is given by Equation E.13. Note once again that the *ansatz* parameters are all real and positive, regardless of model parameter values. This concludes the derivation of free parameters in the two approximants we consider.

We note that a continuous limit $c_\infty \to 0$ to obtain any of the approximants in Table 3.2 is not possible: this is clear from the discrepancy in the order of the dominant term in the long-range asymptotic expansion of V in the case $c_\infty = 0$ (Equation 3.22) vs. $c_\infty \neq 0$ (Equation E.6).

Although the approximant considered here are much simpler than any of the approximants for the case $c_\infty = 0$ summarized in Tables 3.2-3.4, they nevertheless achieve qualitative accuracy in large portions of parameter space, as demonstrated by the combined

buffer concentration error measure results shown in Figure E.1. Finding more accurate approximants for the $c_\infty \neq 0$ is a potential topic of further investigation.

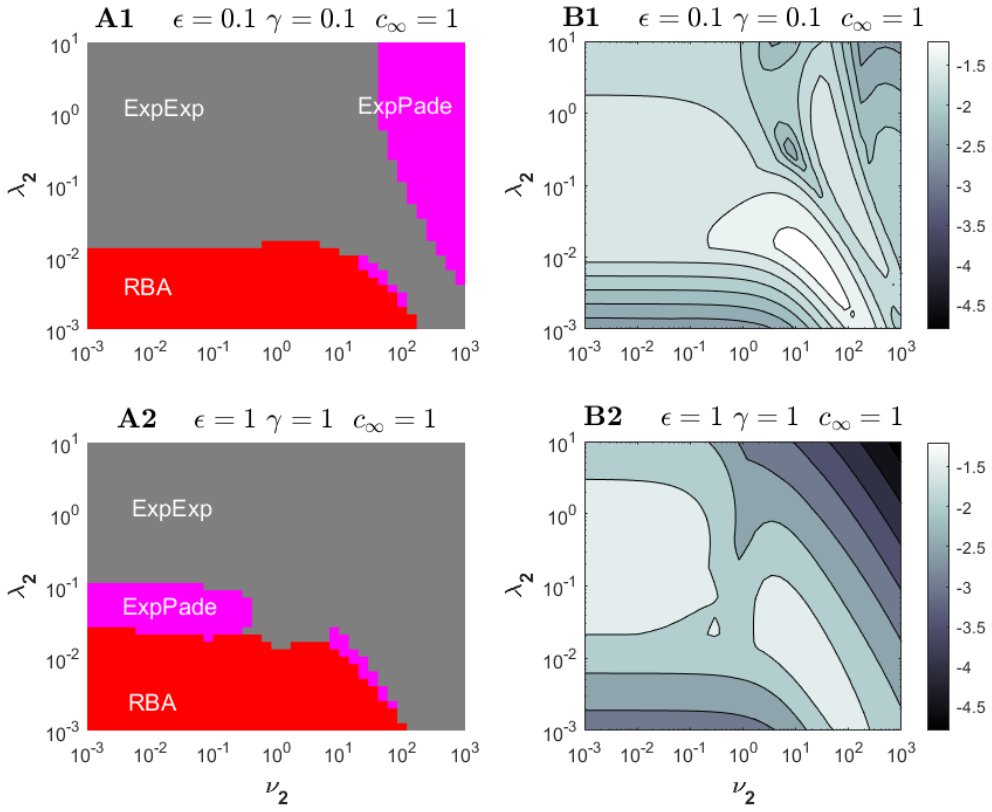

Figure E.1 Best approximants (A1 and A2) and combined accuracy of free and fully bound buffer state approximations (B1 and B2) in the (ν_2, λ_2) parameter plane, as given by the error measure in Equation 3.28, for the case c_∞=1, with parameters ε and γ fixed to two combinations: in A1 and B1, $\varepsilon = \gamma = 0.1$; in A2 and B2, $\varepsilon = \gamma = 1$. Each color in A1 and B1 marks the parameter region of best performance for the following approximants: RBA (*red*), ExpPadé (*magenta*), and ExpExp (*gray*). The color scales in B1 and B2 indicate the log-10 error values. Darker shades represent better accuracy, according to the error bars on the right of each panel.

APPENDIX F

RAPID BUFFERING APPROXIMATION FOR COMPLEX BUFFER

Here we re-derive the Rapid Buffering Approximation in the most general form applicable to both c_∞=0 and $c_\infty \neq 0$ cases. The derivation we give follows the one in (33), but we adapt it to the new and simpler non-dimensionalization considered in this work, whereby the buffer concentrations are re-scaled by the background free buffer concentration, B_∞, rather than the total buffer concentration. This simpler non-dimensionalization allows us to derive the RBA in the most general case of binding-dependent buffer mobility and $c_\infty \neq 0$, whereas these two generalized conditions were only treated separately in (33).

We start by generalizing Equation 3.13 to the case of binding-dependent buffer mobility,

$$\begin{cases} \lambda_1 \nabla_\rho^2 b \;=\; 2\varepsilon c\; b - b^*, \\ \lambda_2 \nabla_\rho^2 b^{**} = \; -c\; b^* + 2b^{**}, \\ \quad b + \delta_B^* b^* + \delta_B^{**} b^{**} = b_T, \\ \quad c + \dfrac{\nu_2}{2}\left(\delta_B^* b^* + 2\delta_B^{**} b^{**}\right) = \dfrac{1}{r} + c_T, \end{cases} \tag{F.1}$$

where the extra parameters characterizing the change of buffer mobility upon Ca^{2+} binding are

$$\delta_B^* = \frac{D_B^*}{D_B}, \quad \delta_B^{**} = \frac{D_B^{**}}{D_B}, \tag{F.2}$$

while the non-dimensional buffer mobility of the fully bound buffer state is redefined according to (cf. Equation 3.15):

$$\lambda_2 = \frac{D_B^{**}}{L^2 k_{1,2}^-}. \tag{F.3}$$

The integration constants in the conservation laws in Equation F.1 are related to the total (fee plus bound) buffer and Ca^{2+} concentrations, and obey a more generalized version of Equations 3.14, 3.17:

$$\begin{cases} b_T = 1 + \delta_B^* b_\infty^* + \delta_B^{**} b_\infty^{**}, \\ c_T = c_\infty + \dfrac{\nu_2}{2}\left(\delta_B^* b_\infty^* + 2\delta_B^{**} b_\infty^{**}\right). \end{cases} \tag{F.4}$$

Since RBA is defined by reaction equilibrium, we equate the reaction terms on the right-hand side of Equation F.1 to zero, which yields (recall that in our non-dimensionalization b_∞=1):

$$\begin{aligned} &b^* = 2\varepsilon c b, \;\; b^{**} = \varepsilon c^2 b, \\ &b_\infty^* = 2\varepsilon c_\infty, \;\; b_\infty^{**} = \varepsilon c_\infty^2. \end{aligned} \tag{F.5}$$

Thus, the buffer conservation laws in Equation F.4 becomes

$$b_T = 1 + \varepsilon c_\infty \left(2\delta_B^* + \delta_B^{**} c_\infty\right) = b\left(1 + \varepsilon c\left(2\delta_B^* + \delta_B^{**} c\right)\right). \tag{F.6}$$

Along with Equation F.5, this gives

$$\begin{cases} b = b_T \Big/ \left[1 + \varepsilon c \left(2\delta_B^* + \delta_B^{**} c \right) \right], \\ b^* = 2\varepsilon c b = 2\varepsilon c b_T \Big/ \left[1 + \varepsilon c \left(2\delta_B^* + \delta_B^{**} c \right) \right], \\ b^{**} = \varepsilon c^2 b = \varepsilon c^2 b_T \Big/ \left[1 + \varepsilon c \left(2\delta_B^* + \delta_B^{**} c \right) \right]. \end{cases} \tag{F.7}$$

Therefore, the Ca^{2+} conservation law in Equation F.1 becomes (recalling that $\varepsilon\nu_2 = \nu_1$)

$$c + \nu_1 c \left(\delta_B^* + \delta_B^{**} c \right) \frac{1 + \varepsilon c_\infty \left(2\delta_B^* + \delta_B^{**} c_\infty \right)}{1 + \varepsilon c \left(2\delta_B^* + \delta_B^{**} c \right)} = \frac{1}{r} + c_T \ , \tag{F.8}$$

where the total $[Ca^{2+}]$ at infinity defined in Equation F.4 becomes

$$c_T = c_\infty \left[1 + \nu_1 \left(\delta_B^* + \delta_B^{**} c_\infty \right) \right]. \tag{F.9}$$

Equation F.8 is readily converted to a cubic equation for c, which has the following real and positive explicit root:

$$c(r) = \frac{S(r)}{A(r)} + A(r) + F(r), \tag{F.10}$$

where the auxiliary quantities A, F, R, S, G depend on model parameters according to

$$\begin{cases} A = \left[\sqrt{R^2 - S^3} + R \right]^{1/3}, \\ R = F\left(F^2 - \dfrac{3G}{2} \right) + \dfrac{1 + c_T r}{2\delta_B^{**} \varepsilon r}, \\ S = F^2 - G, \\ F = \dfrac{1}{3}\left(\dfrac{1}{r} + c_T - b_T \nu_2 - 2\dfrac{\delta_B^*}{\delta_B^{**}} \right), \\ G = \dfrac{1}{3\delta_B^{**}} \left[\delta_B^* \left(\nu_2 b_T - 2\left(\dfrac{1}{r} + c_T \right) \right) + \dfrac{1}{\varepsilon} \right]. \end{cases} \tag{F.11}$$

Here the fractional powers should be understood as the principle root. This expression produces the real positive root when implemented verbatim in MATLAB (Mathworks, Inc.). This result generalizes Equation 19 in (33).

Figures 3.1-3.7 compare this expression with the newly derived approximants and the accurate numerical solution in the special case of binding-independent buffer mobility, $\delta_B^* = \delta_B^{**} = 1$, and zero background Ca^{2+} concentration, c_∞=c_T=0, b_T=1, which simplifies the expressions for auxiliary functions R, F and G in the above expressions:

$$\begin{cases} R = F\left(F^2 - \dfrac{3G}{2} \right) + \dfrac{1}{2\varepsilon r}, \\ F = \dfrac{1}{3}\left(\dfrac{1}{r} - \nu_2 - 2 \right), \\ G = \dfrac{1}{3}\left[\nu_2 - \dfrac{2}{r} + \dfrac{1}{\varepsilon} \right]. \end{cases} \tag{F.12}$$

We note that the asymptotic expansion of the RBA given by Equations E.10-E.12 in powers of x=1/r must agree with Equation 3.22 up to order O(x^3), since the Laplacian in

Equation 3.21 gives asymptotic terms of order O(x^4), while all other terms represent the reaction, which RBA equates to zero.

Figure E.1 shows the RBA results for the case c_∞=1, comparing RBA to two alternative simple closed-form approximants. In that figure, buffer mobility is assumed to be binding independent, so even though the general expression given by Equation E.11 is used, we set $\delta_B^* = \delta_B^{**} = 1$.

APPENDIX G

FROBENIUS ANALYSIS FOR BUFFERED CALCIUM DIFFUSION

Since Equation 2.18 is singular and non-linear, the series expansion solution given by Equation 2.20 has to be carefully justified. Note that Equation 2.18 can be written in the form

$$E[b] = L[b] + \left(\nu b^2 - \eta\right) = 0, \tag{G.1}$$

with $L[b]$ representing the linear part of this equation,

$$L[b_1] = -\lambda\left(\frac{d^2 b_1}{dr^2} + \frac{2}{r}\frac{db_1}{dr}\right) + \frac{1+(\nu-\eta)r}{r} b_1. \tag{G.2}$$

One can use the method of Frobenius to seek solutions of $L[b_1]=0$ of the form

$$b_1(r) = r^{\rho}\sum_{n=0}^{\infty}\beta_n r^n, \tag{G.3}$$

which leads to the lowest-order indicial equation

$$\rho(\rho-1) + 2\rho = \rho(\rho+1) = 0. \tag{G.4}$$

Hence, Frobenius theory implies that the solution given by Equation G.3 is a power series corresponding to the lowest indicial root, ρ=0, with an infinite radius of convergence. Further, it follows from the form of Equation G.1 that it has at least a formal power series solution of the form

$$b(r) = \sum_{n=0}^{\infty} b_n r^n. \tag{G.5}$$

By adapting the usual Frobenius theory, one can prove that this series solution has a non-zero radius of convergence, justifying the Taylor expansion given by Eq. 2.20.

REFERENCES

1. Konieczny, V., M.V. Keebler, and C.W. Taylor. 2012. Spatial organization of intracellular Ca2+ signals. Semin. Cell Dev. Biol. 23: 172–180.

2. Oheim, M., F. Kirchhoff, and W. Stühmer. 2006. Calcium microdomains in regulated exocytosis. Cell Calcium. 40: 423–439.

3. Augustine, G.J., F. Santamaria, and K. Tanaka. 2003. Local calcium signaling in neurons. Neuron. 40: 331–346.

4. Stanley, E.F. 2016. The Nanophysiology of fast transmitter release. Trends Neurosci. 39: 183–197.

5. Berridge, M.J., P. Lipp, and M.D. Bootman. 2000. The versatility and universality of calcium signalling. Nat. Rev. Mol. Cell Biol. 1: 11–21.

6. Neher, E. 2000. Calcium buffers in flash-light. Biophys. J. 79: 2783–2784.

7. Matthews, E.A., and D. Dietrich. 2015. Buffer mobility and the regulation of neuronal calcium domains. Front. Cell. Neurosci. 9: 48.

8. Thurley, K., A. Skupin, R. Thul, and M. Falcke. 2012. Fundamental properties of Ca2+ signals. Biochim. Biophys. Acta. 1820: 1185–1194.

9. Dupont, G., M. Falcke, V. Kirk, and J. Sneyd. 2016. Models of calcium signalling. Cham, Switzerland: Springer International Publishing.

10. Roberts, W.M. 1993. Spatial calcium buffering in saccular hair cells. Nature. 363: 74–76.

11. Simon, S.M., and R.R. Llinas. 1985. Compartmentalization of the submembrane calcium activity during calcium influx and its significance in transmitter release. Biophys. J. 48: 485–498.

12. Fogelson, A.L., and R.S. Zucker. 1985. Presynaptic calcium diffusion from various arrays of single channels. Implications for transmitter release and synaptic facilitation. Biophys. J. 48: 1003–1017.

13. Chad, J.E., and R. Eckert. 1984. Calcium domains associated with individual channels can account for anomalous voltage relations of CA-dependent responses. Biophys. J. 45: 993–999.

14. Neher, E. 1998. Usefulness and limitations of linear approximations to the understanding of Ca++ signals. Cell Calcium. 24: 345–357.

15. Aharon, S., H. Parnas, and I. Parnas. 1994. The magnitude and significance of Ca2+ domains for release of neurotransmitter. Bull. Math. Biol. 56: 1095–1119.

16. Bentele, K., and M. Falcke. 2007. Quasi-steady approximation for ion channel currents. Biophys. J. 93: 2597–2608.

17. Rudiger, S., J.W. Shuai, W. Huisinga, C. Nagaiah, G. Warnecke, I. Parker, and M. Falcke. 2007. Hybrid stochastic and deterministic simulations of calcium blips. Biophys. J. 93: 1847–1857.

18. Smith, G.D. 1996. Analytical steady-state solution to the rapid buffering approximation near an open Ca2+ channel. Biophys. J. 71: 3064–3072.

19. Smith, G.D., L.X. Dai, R.M. Miura, and A. Sherman. 2001. Asymptotic analysis of buffered calcium diffusion near a point source. SIAM J. Appl. Math. 61: 1816–1838.

20. Wagner, J., and J. Keizer. 1994. Effects of rapid buffers on Ca2+ diffusion and Ca2+ oscillations. Biophys. J. 67: 447–456.

21. Bertram, R., G.D. Smith, and A. Sherman. 1999. Modeling study of the effects of overlapping Ca2+ microdomains on neurotransmitter release. Biophys. J. 76: 735–750.

22. Bauer, P.J. 2001. The local Ca concentration profile in the vicinity of a Ca channel. Cell. Biochem. Biophys. 35: 49–61.

23. Naraghi, M. 1997. T-jump study of calcium binding kinetics of calcium chelators. Cell Calcium. 22: 255–268.

24. Naraghi, M., and E. Neher. 1997. Linearized buffered Ca2+ diffusion in microdomains and its implications for calculation of [Ca2+] at the mouth of a calcium channel. J. Neurosci. 17: 6961–6973.

25. Pape, P. C., D.S. Jong, and W.K. Chandler. 1995. Calcium release and its voltage dependence in frog cut muscle fibers equilibrated with 20 mM EGTA. J. Gen. Physiol. 106: 259–336.

26. Stern, M.D. 1992. Buffering of calcium in the vicinity of a channel pore. Cell Calcium. 13: 183–192.

27. Smith, G.D., J. Wagner, and J. Keizer. 1996. Validity of the rapid buffering approximation near a point source of calcium ions. Biophys. J. 70: 2527–2539.

28. Neher, E. 1986. Concentration profiles of intracellular calcium in the presence of a diffusible chelator. In: Calcium Electrogenesis and Neuronal Functioning, Exp. Brain Res. 14, Berlin: Springer-Verlag.

29. Coggins, M., and D. Zenisek. 2009. Evidence that exocytosis is driven by calcium entry through multiple calcium channels in goldfish retinal bipolar cells. J. Neurophysiol. 101: 2601–2619.

30. Nguyen, V., R. Mathias, and G.D. Smith. 2005. A stochastic automata network descriptor for Markov chain models of instantaneously coupled intracellular Ca2+ channels. Bull. Math. Biol. 67: 393–432.

31. Montefusco, F., and M.G. Pedersen. 2018. Explicit Theoretical Analysis of How the Rate of Exocytosis Depends on Local Control by Ca2+ Channels. Comput. Math. Methods Med. 2018: 5721097–12.

32. Trommershäuser, J., R. Schneggenburger, A. Zippelius, and E. Neher. 2003. Heterogeneous Presynaptic Release Probabilities: Functional Relevance for Short-Term Plasticity. Biophys. J. 84: 1563–1579.

33. Matveev, V. 2018. Extension of rapid buffering approximation to Ca2+ buffers with two binding sites. Biophys. J. 114: 1204–1215.

34. Matveev, V. 2016. Pade Approximation of a Stationary Single-Channel Ca2+ Nanodomain. Biophys. J. 111: 2062–2074.

35. Schwaller, B. 2009. The continuing disappearance of "pure" Ca2+ buffers. Cell. Mol. Life Sci. 66: 275–300.

36. Schwaller, B. 2014. Calretinin: from a "simple" Ca(2+) buffer to a multifunctional protein implicated in many biological processes. Front. Neuroanat. 8: 3.

37. Faas, G.C., B. Schwaller, J.L. Vergara, and I. Mody. 2007. Resolving the fast kinetics of cooperative binding: Ca2+ buffering by calretinin. PLoS Biol. 5: e311.

38. Chin, D., and A.R. Means. 2000. Calmodulin: a prototypical calcium sensor. Trends. Cell. Biol. 10: 322–328.

39. Raghuram, V., Y. Sharma, and M.R. Kreutz. 2012. Ca(2+) sensor proteins in dendritic spines: a race for Ca(2+). Front. Mol. Neurosci. 5: 61.

40. Saftenku, E.E. 2012. Effects of calretinin on Ca(2+) signals in cerebellar granule cells: implications of cooperative Ca(2+) binding. Cerebellum. 11: 102–120.

41. Faas, G.C., S. Raghavachari, J.E. Lisman, and I. Mody. 2011. Calmodulin as a direct detector of Ca2+ signals. Nat. Neurosci. 14: 301–304.

42. Kubota, Y., and M.N. Waxham. 2010. Lobe specific Ca2+-calmodulin nano-domain in neuronal spines: a single molecule level analysis. PLoS Comput. Biol. 6(11): e1000987.

43. Falcke, M. 2003. On the role of stochastic channel behavior in intracellular Ca2+ dynamics. Biophys. J. 84: 42–56.

44. Falcke, M. 2003. Buffers and oscillations in intracellular Ca2+ dynamics. Biophys. J. 84: 28–41.

45. Ben Muatjetjeja, and C.M. Khalique. 2011. Exact solutions of the generalized Lane–Emden equations of the first and second kind. Pramana J. Phys. 77: 545–554.

46. Ablowitz, M.J., and A. S. Fokas. 2003. Complex variables: introduction and applications (2nd ed., Cambridge texts in applied mathematics). Cambridge University Press, Cambridge.

47. Evans, L. C. 1998. Partial Differential Equations, Graduate Studies in Mathematics, Vol.19. American Mathematical Society, Providence, RI.

48. Chen, Y., C. Muratov, and V. Matveev. 2020. Efficient approximations for stationary single-channel Ca2+ nanodomains across length scales. bioRxiv. 23: 2020.01.16.909036 (Biophys. J. In Press)

49. Osipov, V.V. 1993. Multifunctional variational method for description of evolution and dynamics of dissipative structures in nonequilibrium systems. Phys. Rev. E. 48: 88–100.

50. Bensoussan, A., and J. Frehse. 1984. Nash point equilibria for variational integrals. In: Vinti C. (eds) Nonlinear Analysis and Optimization. Lecture Notes in Mathematics, vol 1107. Springer, Berlin, Heidelberg.

51. Gordon, P.V., C.B. Muratov, and S.Y. Shvartsman. 2013. Local accumulation times for source, diffusion, and degradation models in two and three dimensions. J. Chem. Phys. 138: 104121.